

THE RELATIONSHIP BETWEEN STELLAR LIGHT DISTRIBUTIONS OF GALAXIES AND THEIR FORMATION HISTORIES

CHRISTOPHER J. CONSELICE¹

Henry Robinson Laboratory for Astrophysics, California Institute of Technology, MS 105-24, Pasadena CA 91125

To Appear in Astrophysical Journal Supplements (July 2003)

ABSTRACT

A major problem in extragalactic astronomy is the inability to distinguish in a robust, physical, and model independent way how galaxy populations are related to each other and to their formation histories. A similar, but distinct, and also long standing question is whether the structural appearances of galaxies, as seen through their stellar light distributions, contain enough physical information to offer this classification. We argue through the use of 240 images of nearby galaxies that three model independent parameters measured on a single galaxy image reveal its major ongoing and past formation modes, and can be used as a robust classification system. These parameters quantitatively measure: the concentration (C), asymmetry (A) and clumpiness (S) of a galaxy's stellar light distribution. When combined into a three dimensional 'CAS' volume all major classes of galaxies in various phases of evolution are cleanly distinguished. We argue that these three parameters correlate with important modes of galaxy evolution: star formation and major merging activity. This is argued through the strong correlation of $H\alpha$ equivalent width and broad band colors with the clumpiness parameter, the uniquely large asymmetries of 66 galaxies undergoing mergers, and the correlation of bulge to total light ratios, and stellar masses, with the concentration index. As an obvious goal is to use this system at high redshifts to trace evolution, we demonstrate that these parameters can be measured, within a reasonable and quantifiable uncertainty, with available data out to $z \sim 3$ using the Hubble Space Telescope GOODS ACS and Hubble Deep Field images.

Subject headings: Galaxies: Evolution, Formation, Structure, Morphology, Classification

1. INTRODUCTION

The most basic process in any observational science is the classification of objects under study into a taxonomy system. Advances in scientific fields such as biology and chemistry have historically depended upon the correct interpretation and ordering of objects according to similar, or dissimilar, physical processes or characteristics. In 20th century astronomy, the classification of stars via an interpretation through color-magnitude diagrams led to the correct picture, and new ideas, for how stars form and evolve. This has further led to an increase in our understanding of stellar systems, most notably star clusters and galaxies. A primary concern in astronomy today is determining how galaxies have formed, evolved, and are evolving. The limited progress in our understanding of this is due in no small part to our inability to identify distinct galaxy populations over a range of redshifts based on their fundamental features. If the correct distinctions can be made, the salient effects of galaxy evolution can be sorted out and studied, and galaxy formation scenarios should rapidly follow.

It is also often believed that galaxy classification systems are in many ways not very useful for determining evolution. This is the direct result of the most popular classification systems having non-physical and often purely descriptive classification criteria based on optical morphologies that do not uniquely identify, or distinguish, galaxies in different modes of evolution (Appendix A). This classification crisis is in part the result of the high fraction of distant galaxies that look peculiar in deep Hubble Space

Telescope (HST) images (e.g., Glazebrook et al. 1995; Abraham et al. 1996) and which cannot be placed onto the Hubble sequence. An ideal galaxy classification system is one that classifies objects on the basis of their most important physical features, which the most commonly used morphological systems do not (see Appendix A).

So-called physical morphologies are not new, and attempts to construct a meaningful system for galaxies started with the work of Morgan (1958, 1959) who attempted to correlate "the forms of certain galaxies and their stellar content as estimated from composite spectra" from Morgan & Mayall (1957). Later attempts include e.g., van den Bergh's (1960) study of the correlation between spiral arm structure and intrinsic galaxy brightness and Morgan and Osterbrock's (1969) classification of galaxies in terms of dominant stellar populations. Modern studies have attempted to classify ellipticals by their internal structures (Kormendy & Bender 1996) and through using interacting and star formation properties (e.g., Conselice 1997; Conselice et al. 2000a (hereafter CBJ00); Conselice et al. 2000b; Bershady et al. 2000). Others have used quantitative features for classification, but without trying to understand the physical basis of the measured quantities (e.g., Abraham et al. 1996; Naim, Ratnatunga & Griffiths 1997). However, none of these systems provide a solid useful frame work for classifying galaxies in a manner tied to underlying physical processes or properties.

We argue two main points in this paper. First, we show that galaxies in different stages of evolution can be distinguished using only three computationally computed struc-

¹NSF Astronomy & Astrophysics Postdoctoral Fellow

tural indexes. These three parameters are: the concentration of stellar light (C), its asymmetric distribution (A), and its clumpiness (S). All galaxies fall in various locations of a volume created using these three structural indices (hereafter CAS volume). Second, we argue that the values of the CAS parameters directly measure the major current and past modes of galaxy formation and evolution. We discuss evidence that the concentration index traces the past evolutionary history of galaxies and potentially correlates with the fraction of stars produced through gas accreted from the intergalactic medium, as opposed to stars put into place through a gravitational infall of gas and pre-existing stars. We further argue that the asymmetry and clumpiness parameters reveal active evolution resulting from recent major mergers and star formation, respectively, while the concentration index is the ratio of the integral of these processes. The major conclusion from this study is that the structural appearance of nearby resolved galaxies, at only a single observed optical wavelength, is suitable for understanding their current and past evolutionary history. The CAS system can therefore be used to uniquely and automatically identify galaxies of all major morphological types out to $z \sim 3$, including those on the Hubble sequence.

This paper is organized as follows: §2 is a discussion of galaxy structure and its potential usefulness and limitations for uncovering evolutionary processes in galaxies. §3 describes the 240 galaxies used in this paper to determine the usefulness of the CAS system and §4 is a description of the CAS parameters while §5 demonstrates how these parameters correlate with fundamental galaxy properties. §6 describes how the CAS parameters can be used, independent of any physical meaning, to classify and separate all galaxies into distinct types and argues that we can use the CAS system at high redshift, and §7 is a summary.

2. THE USE OF GALAXY STRUCTURE: WHY A NEW SYSTEM IS NEEDED

When examining the spatial structure of a galaxy in optical, ultraviolet or infrared light, its appearance is dominated by stars, but effects from ionized gas and dust play a role, as does projection. In addition to this we have the issue of projection, that is, we view galaxies as two dimensional ‘pictures’ when in fact stars are distributed in a galaxy in three dimensional space. When trying to understand a galaxy from its stellar light distributions, and what it means physically, all of the above effects must be taken into account.

The apparent distribution of stellar light in nearby bright galaxies quickly led to the Hubble classification system (Hubble 1926) which has remained, until recently, the dominant method for understanding galaxy populations. In the last few years however it has been demonstrated that classifying galaxies only using the Hubble sequence has its limitations (see Appendix A). While nothing a priori should have suggested this - the fundamental properties of a galaxy are not uniquely revealed through Hubble type classification criteria, i.e., spiral arms and bars. As such, a new classification system which is automated, robust at all redshifts, and which correlates with the major physical processes occurring in galaxies is now desperately needed, especially with the advent of the Advanced Camera for Surveys (ACS) and in the near future WFPC3,

both Hubble Space Telescope imaging instruments. We briefly consider the various options for constructing such as physical morphology below.

2.1. Sizes and Shapes

The most basic structural property of a galaxy is its size, and its two dimensional shape. The correlation between the sizes and masses of galaxies suggests that to first order the size of a galaxy is an important clue for understanding origins. Sizes however depend upon knowledge of the distances to galaxies, something that is often not know.

The importance of the three dimensional shape of a galaxy in terms of its formation and evolutionary history is not yet entirely clear. Statistically, we know that ellipticals and disks must have different shapes, with disks on average flatter (Lambas, Maddox & Loveday 1992). Inversion techniques of the distribution of apparent axial ratios also show that elliptical galaxies are neither prolate or oblate, but triaxial in shape (Lambas et al. 1992; Ryden 1996), consistent with a lack of significant rotation (Bertola & Capaccioli 1975; Franx, Illingworth & de Zeeuw 1991).

In any case, the detailed three dimensional shape of early type systems may not be critically important for understanding their stellar content and evolution. This is especially the case for elliptical galaxies which have little dust (White, Keel & Conselice 2000) and we obtain a clean ‘view’ of its stellar populations projected onto two dimensions. The three dimensional shape of a spiral galaxy is often inferred from images to be rotationally supported disks, an idea confirmed by their large rotational components (Sofue & Rubin 2001). Despite the fact that some disks are optically thick with high internal extinctions (White et al. 2000) these galaxies have patchy dust distributions, and therefore we are not likely missing a significant amount of light when galaxies are projected onto two dimensions. Later in this paper, and in CBJ00, we discuss quantitatively how the inclination of spiral galaxies effects measured morphological properties. We find that although projection effects are important, their effect on structure and morphology be can dealt with, and corrected for, in a quantitative way (CBJ00, §4.3).

2.2. Light Decompositions

Understanding the morphology of a galaxy through the decomposition of its light profile is perhaps the most popular method of quantifying galaxy light distributions (e.g., Peng et al. 2002; Simard et al. 2002). These decompositions are done by fitting a model to surface brightness profiles, either one or two dimensional. Typically these models are based on various fitting forms, such as the de Vaucouleurs, exponential or Sérsic profiles, and sometimes also including fitting central point sources (Peng et al. 2002).

These light decompositions are attractive due to their ability to ‘fit’ and quantify light in ‘bulge’ and ‘disk’ components which are thought to define the Hubble sequence (Appendix A), although these methods have several problems, both philosophical and technical. The most important issue is that bulge and disk decompositions are only useful for quantifying the structures of galaxies with well defined and a priori assumed morphologies, namely galaxies with roughly smooth and symmetric light profiles. There are also issues involving the nature of the

fitting process which assumes the form of the light profile and therefore any morphological information is model dependent. Galaxies at high redshifts have peculiar structures that cannot be fit by these assumed profiles. Since these models are azimuthally smoothed averages, they do not account for effects caused by star formation or mergers which can distort a galaxy's light distribution.

It has also not yet been demonstrated that bulge + disk (B/D) decompositions are unique descriptions of galaxy light profiles. Observations indicate (MacArthur, Courteau & Holtzman 2003) that normal disk galaxies come in several types such that the relationship between bulge and disk light may not be as simple as these model fitting techniques assume. It is also not clear that bulges are well fit by the de Vaucouleur profile, with significant evidence that they are not (Andredakis & Sanders 1994; MacArthur et al. 2003). If one does not assume a de Vaucouleur or exponential form, but use the more general Sérsic profile, the minimization is over at least a dozen parameters and can result in many different possible solutions. This is well known, and B/D decompositions are likely only useful to some degree for bright nearby galaxies (e.g., MacArthur et al. 2003). The Sérsic index is also probably not always the best description of a galaxy's light profile. We investigate this further by modeling the light profiles of galaxies on the Hubble sequence and compute B/D ratios, and use these to determine how these relate to our model independent parameters.

What is needed is a galaxy classification methodology that does not rely on any assumptions about galaxy light distributions and correlates with the major physical processes occurring in galaxies. This paper argues that such a system can be constructed based on measuring how stars are distributed in galaxies through the CAS system.

3. DATA AND ANALYSIS OF NEARBY GALAXIES

To develop our CAS physical morphology we study optical digital CCD images of nearby galaxies in various phases of evolution taken from many different inhomogeneous data sets. These include normal galaxies (ellipticals and spirals), starburst galaxies, dwarf irregulars, dwarf ellipticals and galaxies undergoing merging. Each of these separate data sets is briefly described below.

3.1. *Frei Sample - Nearby Normal Galaxies*

The Frei et al. (1996; hereafter Frei) sample is a collection of 113 nearby normal galaxies of all classical Hubble types from ellipticals to irregulars whose quantitative morphological properties are listed in Table 1 (see also CBJ00 and Bershady et al. 2000 for additional physical data on these systems). Two telescopes were used to acquire these images; the Lowell 1.1m and the Palomar 1.5m. For the Lowell sample we use the R-band images and we use the g-band image from the Palomar sample in our morphological analysis. We refrain from a detailed description of the morphological properties of these galaxies, as this has been done in detail elsewhere (e.g., Frei et al. 1996; CBJ00; Bershady et al. 2000). It is sufficient to state that the Frei sample is a good representation of nearby large bright galaxies, but is deficient in low-luminosity systems (§3.3) and galaxies in unusual modes of evolution, such as massive star formation events (§3.2) and galaxy mergers (§3.4).

3.2. *Star-Forming Galaxies*

As a significant fraction of galaxies at high redshifts show morphological and physical evidence for undergoing higher than average star formation as compared to galaxies in the nearby universe, we examine the morphological properties of five nearby starburst galaxies that are generally regarded as the best analogs of high redshift star-forming systems (e.g., Conselice et al. 2000b,c). These five galaxies have been discussed in detail in Conselice et al. (2000c). As a significant fraction of star formation in the high- z universe is thought to occur in galaxies that are brightest in the infrared, we also investigate a sample of ultra luminous infrared galaxies that are proposed to be the nearby analogs to high- z sub-mm sources (e.g., Blain et al. 1999) (see §3.4).

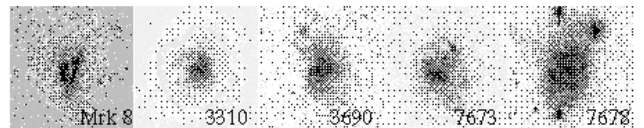


FIG. 1.— Images of the Starburst sample whose properties are listed in Table 2.

Images of these UV bright starbursts are shown in Figure 1 and were all observed with the WIYN 3.5 m telescope in 1998 with the S2kB CCD detector (see Conselice et al. 2000b,c for details of the observations). We use Harris R-band images of each galaxy in our morphological analyses, the results of which are listed in Table 2. Before performing the structural parameter measurements on these starbursts, all contaminating features such as foreground stars, background galaxies, cosmic rays, and light gradients were removed (Conselice et al. 2000b).

3.3. *Dwarf Elliptical and Irregular Galaxies*

Low-mass, or dwarf, galaxies are the most common galaxy type in the nearby universe, and are particularly abundant in galaxy clusters (e.g., Ferguson & Bingelli 1994; Conselice et al. 2001,2002,2003). Any classification system that claims to account for all galaxies should accommodate these low-mass systems, something the Hubble sequence does not do (see Appendix A). As such we include a sample of 19 dwarf elliptical galaxy images selected from the sample of Conselice et al. (2003) (Table 3) and 37 dwarf irregulars from the sample of van Zee (2000) (Table 4). Like the starburst sample, these dE galaxies were imaged using the WIYN telescope with the S2kB detector in the Harris R-band. The observational details for these galaxies is described in Conselice et al. (2003a).

The dwarf irregular sample are B-band images taken with the 0.9m telescope at the Kitt Peak National Observatory whose reduction and sample properties are described in van Zee (2000). These galaxies were selected by van Zee (2000) to have $M_B > -18$, a late-type morphology, and specific HI criteria (see van Zee 2000). We do not use all the B-band images from this sample, as some are near bright stars, making a careful analysis of morphology difficult. The 37 galaxies from this sample that we use are listed in Table 4. We apply a slight morphological k-correction, based on the Frei galaxy's B and R morphologies, to convert the B-band CAS values of these irregulars

into pseudo-R band values. These corrections are however very slight ($\delta C = 0.12, \delta A = -0.03, \delta S = -0.03$) and do not effect the results in any significant way. The B-band CAS values for these dwarf irregulars are listed in Table 4.

3.4. Luminous IR Galaxy Sample - Mergers

Luminous and ultraluminous infrared galaxies (LIRGs) and (ULIRGs) are objects that emit most of their light in the infrared (IR) at $\lambda = 2\mu - 100\mu$ (Rieke & Low 1972) with luminosities $L_{IR} > 10^{11} L_{\odot}$ (Sanders & Mirabel 1996). LIRGs and ULIRGs are among the most luminous objects in the nearby universe bolometrically and in particular at wavelengths from $8 - 100\mu\text{m}$. The general idea is that these galaxies are for the most part recent mergers (Sanders et al. 1988; Borne et al. 2000; Canalizo & Stockton 2001) with induced star formation and AGN activity which produces energetic photons that are absorbed by dust and later thermally re-emitted in the infrared by heated grains. To address some questions concerning these galaxies several groups obtained HST images of LIRGs and ULIRGs in the F814W (hereafter I) and F555W (hereafter V) bands. We use these samples to study the morphological properties of merging galaxies, which are much more common at high redshifts than in the nearby universe (e.g., Conselice et al. 2003b).

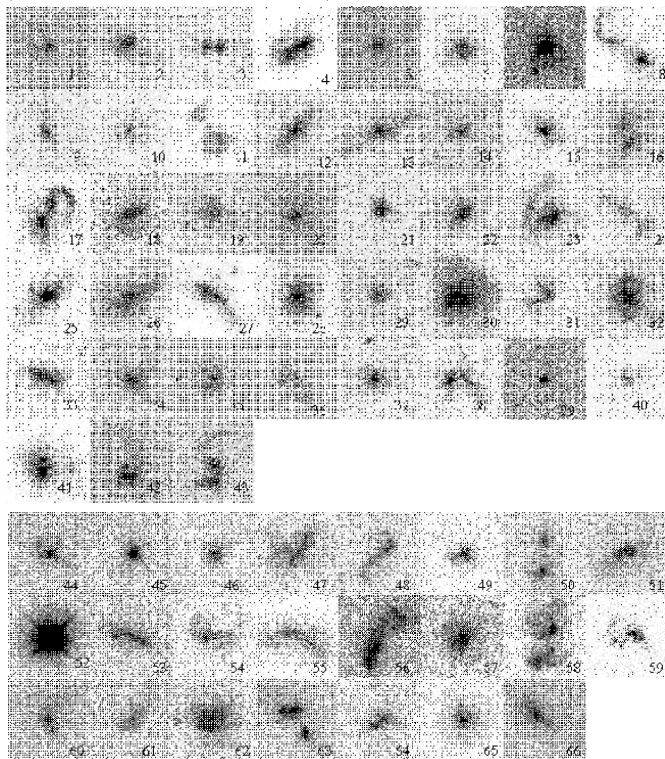


FIG. 2.— Images of the luminous and ultraluminous infrared sample whose properties are listed in Table 5.

Table 5 and Figure 2 list the data and display the images for the 66 ULIRGs in these two imaging sets (HST IDs 6346 and 6356). We list separately, in Table 5, galaxies from these two programs as they use different filters and exposure times. The 43 galaxies taken in the I band were obtained in two separate 400 second WFPC2 exposures and two 300 second WFPC2 exposures were acquired for the V-band data. For cosmic ray removal the IRAF task CRREJ was used, and the two frames combined. We

refer to Borne et al. (2000) and Ferrah et al. (2001) for alternative descriptions of these galaxies. As in the dE and starburst samples, before we apply our morphological techniques we remove any contaminating features near the galaxies in question, such as other smaller background galaxies, foreground stars and any cosmic rays not removed by the combination of the two separate exposures. The computed CAS parameters for these galaxies are listed in Table 5 in the rest-frame F814W and F606W wavebands. To compare these values properly with the R-band images used for the rest of the sample, we perform a quantitative morphological k-correction to estimate the rest-frame R band values of each CAS parameter (see also §3.3). This is done by first computing the observed wavelength for each galaxy using the filter observed (F814W or F606W) and the redshift of the galaxy, which is listed in Table 5. After this is done, the difference in the sampled rest-frame wavelength at F814W or F606W and rest-frame R-band at 650 nm is computed and a morphological k-correction is calculated and applied. The value of this correction is found through an extrapolation based on a calibration between the morphological parameters of the Frei sample in the B and R bands.

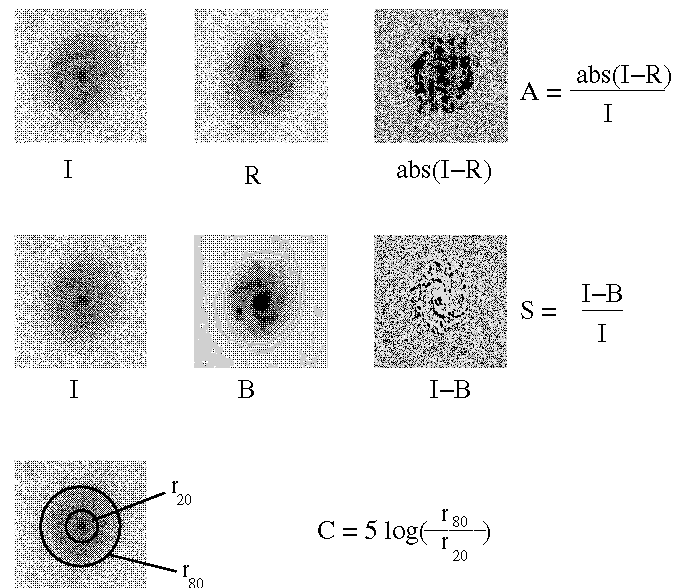


FIG. 3.— Graphical representation of how the three parameters used in this paper, asymmetry (A), clumpiness (S) and concentration (C) are measured. For the measurements of A and S , I is the original galaxy image, R is this image rotated by 180° , while B is the image after it has been smoothed (blurred) by the factor $0.3 \times r(\eta = 0.2)$. The details of these measurements are not shown here but can be found in Conselice et al. (2000a) for asymmetry, A , Bershady et al. (2000) for concentration, C , and this paper for the clumpiness index, S .

4. THE CAS STRUCTURAL PARAMETERS

This section describes how the CAS parameters used in this study are computed. Figure 3 is a very basic graphical representation of how the concentration, asymmetry and clumpiness parameters are measured. There are possibly better ways to measure these parameters to strengthen correlations with physical properties. In some cases actually measuring the physical quantities traced by the CAS indices, such as star formation, can supersede the use of any morphologies. It is hoped that this paper will in-

fluence others to investigate different possibilities, such as more automated methodologies of measuring galaxy structures through e.g., shapelets (e.g., Massey et al. 2003). Later in the paper we discuss what internal physical properties the CAS parameters correlate with, and construct a three-dimensional structural space and show that all major nearby galaxy types can be cleanly distinguished within this volume.

4.1. Concentration of Light

Light concentration is an often used feature in galaxy classification studies, and has been used qualitatively previously in the Hubble system, and in various alternative classification schemes (e.g., Morgan & Mayall 1957). Briefly, elliptical galaxies are the most concentrated systems, and the concentration of stellar light decreases for later Hubble types (e.g., Bershady et al. 2000). Disk galaxies with large rotational velocities, and high angular momenta, have lower light concentrations (e.g., Bershady et al. 2000), as do dwarf galaxies (Conselice et al. 2002). We further discuss the relationship between concentration and physical properties of galaxies in §5.

Measuring the light concentration quantitatively can be done by using a single index which has been described in detail in many papers, using a variety of different techniques (e.g., Morgan & Mayall 1957; Okamura, Kodaira & Watanabe 1984; Kent 1985; Doi, Fukugita & Okamura 1993; Abraham et al. 1994; Bershady et al. 2000; Graham, Trujillo & Caon 2001). In this paper the same methodology described in Kent (1985) and Bershady et al. (2000) is used. This concentration index is a number, C , defined as the ratio of the 80% to 20% curve of growth radii (r_{80} , r_{20}), within 1.5 times the Petrosian inverted radius at $r(\eta = 0.2)$, normalized by a logarithm,

$$C = 5 \times \log(r_{80\%}/r_{20\%}).$$

See Bershady et al. (2000) for a full description of how this parameter is computed. The asymmetry (§4.2) and clumpiness (§4.3) parameters are also measured within the $1.5 \times r(\eta = 0.2)$ radius (see CBJ00 for a discussion of the benefits of using this particular value). The quantitative values of C range from roughly 2 to 5 with most systems having $C > 4$ ellipticals, or spheroidal systems in formation, with disk galaxies at values generally between $4 < C < 3$. The lowest concentrated objects are those with low central surface brightnesses, and low internal velocity dispersions (Graham et al. 2001; Conselice et al. 2002a).

4.2. Asymmetry

The asymmetry index, A , has been used previously to quantify the morphologies of galaxies, usually those seen at high redshift (e.g., Shade et al. 1995; Abraham et al. 1996; Brinchmann et al. 1998; Conselice et al. 2003b). However, there are only a few previous attempts to calibrate and characterize an asymmetry index on nearby galaxies, and models of galaxy formation, to understand its importance for measuring galaxy evolution (Conselice 1997; Conselice et al. 2000a,b; Conselice 2000; Conselice et al. 2001).

²Ideally a measurement of the global asymmetry would be computed by considering all light from a galaxy equally. That is, all pixels in a galaxy are given a binary value of 1 or 0 depending on whether or not light is being emitted from the galaxy at each respective pixel. This is decided by determining if pixel values are greater than, or less than, some level of the sky variation σ . Everything less than $n\sigma$ is set to zero while everything greater than $n\sigma$ is set to 1 and is presumably a pixel that samples part of the galaxy. Although this method was tried

The asymmetry index is defined as the number computed when a galaxy is rotated 180° from its center and then subtracted from its pre-rotated image, and the summation of the intensities of the absolute value residuals of this subtraction are compared with the original galaxy flux. There are further corrections applied for removing the background, and well-defined radii and centering algorithms (see CBJ00 for a full detailed description). The asymmetry index used in this paper, as defined in CBJ00, is sensitive to any feature that produces asymmetric light distributions. This includes star formation, galaxy interactions/mergers, and projection effects such as dust lanes. Since most galaxies are not edge-on systems, star formation and galaxy interactions/mergers are likely the dominant physical effects (CBJ00). While no non-mergers have very high asymmetries the corollary is not true, and galaxies that have undergone a merger can have modest asymmetry values (see §5.2.1). Asymmetry also tends to correlate with the $(B - V)$ color of galaxies, an indication that it is sensitive to some degree to the ages of a galaxy's stellar populations.

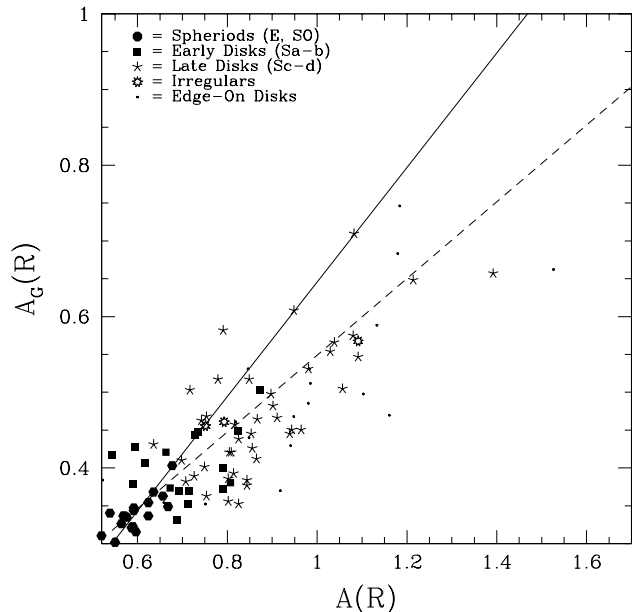


FIG. 4.— The global asymmetry parameter $A_G(R)$ plotted as a function of the asymmetry parameter $A(R)$. The dashed line is a best fit between these two parameters, while the solid line shows the relationship $A_G(R) = A(R)$.

It would be ideal to have an asymmetry index sensitive only to large scale stellar distributions. To measure this we compute the asymmetries of each galaxy image in our sample after it is convolved with a smoothing filter of size $1/6 \times r(\eta = 0.2)$, to reduce the image's effective resolution. The asymmetry of this smoothed galaxy is then computed in the normal manner (CBJ00). We call this value the global asymmetry, $A_G(R)$. This is equivalent to studying the asymmetric components of a galaxy's low-frequency structure.²

Figure 4 shows the relationship between the global asymmetry, $A_G(R)$ and the total asymmetry $A(R)$ for the Frei sample. There is a very good correlation between these two parameters, such that

$$A_G(R) = (0.67 \pm 0.05) \times A(R) + (0.01 \pm 0.01). \quad (1)$$

Based on this, only $\sim 30\%$ of galactic asymmetries can be produced by high frequency structures, such as star formation. Because the asymmetry of a galaxy generally does not decrease strongly with decreased resolution, its asymmetric structures are likely caused by global distortions. If star formation was a significant factor in producing asymmetries, the A_G values would decrease significantly from the original A value. Since they do not, as was also argued in CBJ00, it is likely that star formation is not producing a large asymmetry signal, and we simply use the pure asymmetry index, $A(R)$, to obtain an estimate of global asymmetries.

4.3. The High-Spatial Frequency Clumpiness Parameter (S)

The light distribution in a galaxy can be roughly characterized by three features: its integrated light distribution, the rotational symmetry of this distribution and the patchiness of this distribution (Appendix B). The first two are described by the well studied asymmetry and concentration indices, while the third can be measured with a parameter introduced here, which we call the clumpiness (S). Earlier work on similar techniques includes investigations by Isserstedt & Schindler (1986) and Takamiya (1999).

There are several ways a galaxy can contain clumpy material at high-spatial frequencies. Ellipticals, for example, usually do not have any high-spatial frequency power in their structures. Most ellipticals are ‘smooth’ and therefore only contain low-frequency, or a nearly DC low-power structure. However, galaxies undergoing star formation are very patchy and contain large amounts of light at high-frequency. To quantify this, we define the clumpiness index (S) as the ratio of the amount of light contained in high frequency structures to the total amount of light in the galaxy. For ellipticals this ratio should be, and generally is, near zero.

After experimentation the best and most simplistic way to measure the high spatial frequency components in a galaxy was found. The computational method is simple: the original galaxy’s effective resolution, or ‘seeing’ is reduced to create a new image. This is done by smoothing the galaxy by a filter of width σ . The effect of this is to create an image whose high-frequency structure has been washed out. This can also be thought of as lowering the ϵ resolution parameter of CBJ00 such that one seeing element contains some fraction of a galaxy’s radius. The original image is then subtracted by this new reduced resolution image. The effect of this is to produce a residual map that contains only the high frequency components of the galaxy’s stellar light distribution (see Figure 3). The flux

using several σ values and various radii, the best turned out to be a 3σ division. The resulting image then contains only pixels with values 0 or 1. The global asymmetry index was then computed using the same techniques presented in CBJ00. However, after extensive testing it was found that this procedure was not robust, and gave global asymmetry measurements that correlated strongly with the type of galaxy, with elliptical galaxies usually having the highest values due to the systematics caused by their extensive surface brightness envelopes. Therefore this methodology was rejected for further use.

of this residual light is then summed and divided by the sum of the original galaxy image flux to obtain a galaxy’s clumpiness (S) value. If the subtraction process results in few residuals, it implies that the galaxy contains little light at high frequencies and the S index is near zero. On the other hand, if a significant fraction of the light in a galaxy originates from these high-frequency clumpy components, the S index will be large. Computationally S is defined as:

$$S = 10 \times \frac{\sum_{x,y=1}^{N,N} (I_{x,y} - I_{x,y}^\sigma) - B_{x,y}}{I_{x,y}} \quad (2)$$

where $I_{x,y}$ is the sky subtracted flux values of the galaxy at position (x,y) , $I_{x,y}^\sigma$ is the value of the galaxy’s flux at (x,y) once it has been reduced in resolution by a smoothing filter of width σ , and N is the size of the galaxy in pixels. The value $B_{x,y}$ is the background pixel values in an area of the sky which is equal to the galaxy’s area. Computationally the clumpiness index, S , has additional measurement features. The inner part of each galaxy is not considered in the computation of S as these are often unresolved and contain significant high-frequency power that is unrelated to the stellar light distribution, but an artifact of finite sampling. We also force any negative pixels, that is parts of a galaxy that are over subtracted in equation (2), to zero before computing S . We also use a smoothing filter of size $\sigma(I) = 1/5 \times 1.5 \times r(\eta = 0.2) = 0.3 \times r(\eta = 0.2)$, although in principle any scale can be used to measure various frequency components in a galaxy. The S values for our various galaxy types are listed in Tables 1 - 5.

5. PHYSICAL INTERPRETATION OF THE CAS PARAMETERS

5.1. Light Concentration - Scale and Past History

In major galaxy formation scenarios the concentration of a galaxy’s light strongly depends upon its formation history, that is how its stars were put into place. In hierarchical galaxy formation scenarios elliptical galaxies and spiral bulges form by the mergers of pre-existing stellar and gaseous systems which lose angular momentum through the ejection of tidal tails of material. This results in high stellar light concentrations. Alternatively, in a monolithic collapse scenario, stars are concentrated in an elliptical galaxy or in a bulge due to the rapid collapse of gas that quickly forms stars in less than 100 Myrs, or from a rapid collapse of pre-existing stars. In these models the resulting spheroids can then acquire a disk from star formation produced from gas deposited from the intergalactic medium that cools onto the spheroid (Steinmetz & Navarro 2002). After the gas inside each halo cools, its angular momentum determines the properties of the formed disk including its light concentration, which will be lower than systems formed through a rapid gravitational collapse.

Does the concentration index really tell us about any fundamental galaxy properties, or how a galaxy has formed? A galaxy’s light concentration has been shown since Okamura, Kodaira & Watanabe (1984) to correlate

with the internal properties of galaxies, notably Hubble types and surface brightness. Recent studies have also shown that light concentration indices correlate with internal scaling properties such as velocity dispersion, galaxy size, luminosity and black hole mass (Graham et al. 2001). There are also various definitions of the concentration index, such as the central light concentration (Graham et al. 2001) that correlate better with some of these parameters. Investigating various light concentration indices, including which is the best for measuring scale features is beyond the scope of this present paper, but see Graham et al. (2001) for a good discussion of these issues.

5.1.1. Concentration vs. Bulge to Total Light Ratios

The concentration index we use does however correlate with several internal galaxy properties. First, the concentration index scales with the bulge to total light flux ratios (B/T) for nearby normal galaxies (Figure 5), although there is a large scatter, particularly for early type disk galaxies. We measure these B/T ratios for the sample of normal Hubble sequence galaxies in the Frei sample using the GALFIT fitting software (Peng et al. 2002). GALFIT is a 2-dimensional bulge + disk χ^2 minimization program that finds the best de Vaucouleur and exponential profile fit to the light distribution of a galaxy (Peng et al. 2002). Figure 5 shows the relationship between C and B/T whose best fit relationship is,

$$B/T = (0.4 \pm 0.03) \times C + (-0.88 \pm 0.11). \quad (3)$$

The concentration index can thus be used as an indicator of a galaxy's gross form (i.e., elliptical or spiral), within some scatter. The origin of this scatter is not clear as the residuals of the linear fit in eq. (3) do not correlate with the inclination, asymmetry or any other morphological feature.

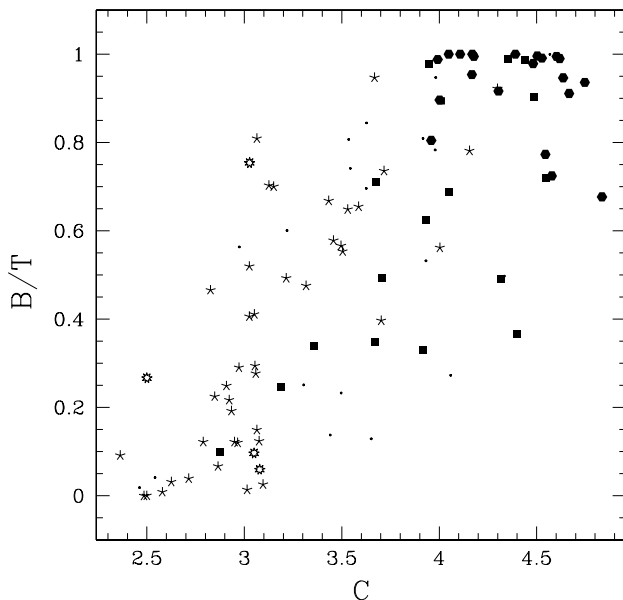


FIG. 5.— Bulge to total light ratios for the Frei sample as a function of the total light concentration. The symbols here have the same meaning as in Figure 4.

As shown in Graham et al. (2001) the concentration in-

dex is also a measure of the scale of a galaxy, whereby we mean the size, absolute magnitude or mass, as defined in Bershady et al. (2000). Graham et al. (2001) argue that the central concentration of light is a better measure of scale than total light concentration, although there is still a correlation between the total light concentration and the stellar mass, as given by the factor $M_B - (M/L)_B$, where $(M/L)_B$ is the stellar mass to light ratio in the B-band estimated from the $(B - V)$ color of each galaxy (Worthey 1994). When we compare this value to the concentration index, C , we find a general correlation, with an average scatter of one magnitude (Figure 6). This relationship is:

$$M_B = (-2.0 \pm 0.3) \times C + (-14.2 \pm 1.1). \quad (4)$$

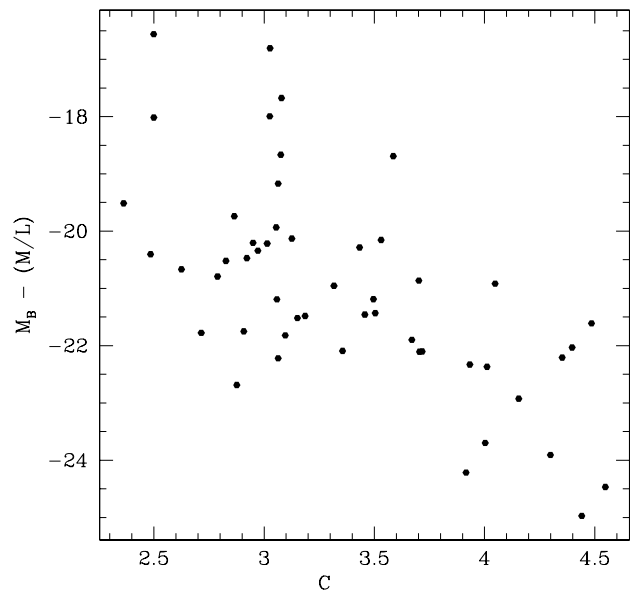


FIG. 6.— The relationship between the concentration index, C , and $M_B - M/L$ for the nearby normal galaxies in the Frei sample.

Based on this, and the results of Graham et al. (2001), it seems very likely that the scatter shown in Figure 6 can be significantly reduced by using either a refined concentration index, or through the use of a careful analysis using a third morphological parameter that effects light concentration, such as inclination or star formation.

5.2. Asymmetry - Mergers

Galaxy interaction and merger rates, and the fraction of galaxies involved in mergers, is predicted in hierarchical models to increase as a function of redshift (e.g., White & Frenk 1991; Lacey & Cole 1993; Cole et al. 2000). Mergers in this scenario build up the masses and structures of galaxies. Observations suggest that mergers are indeed more common at higher redshifts (Conselice et al. 2003b).

Despite this, the importance of galaxy mergers in the galaxy evolution process is still debated, although galaxy mergers are clearly occurring. The effects of past merging activity is easily seen in the local galaxy population. For example, Fourier analyses of nearby galaxy structures reveal that over 30% of spirals show evidence for recent accretion events (Zaritsky & Rix 1997). Our own galaxy and M31 also contain evidence for past merging events,

such as a heated thick disk and stellar streams that are likely the result of accretion of satellites (Quinn, Hernquist & Fullagar 1993; Gilmore, Wyse & Norris 2002). Evidence for past mergers can also be found in the outer parts of galaxies where dynamical time scales are long, and where apparently normal galaxies have evidence for past merger activity in the form of stellar shells (Schweizer & Seitzer 1992) and HI asymmetries and warps (Sancisi 1976; Richter & Sancisi 1994). While many galaxies have some clues left over from past merging events, these can be quite diverse, and require various methods to retrieve, many of which are expensive in telescope time, and hard to impossible to measure at high redshifts.

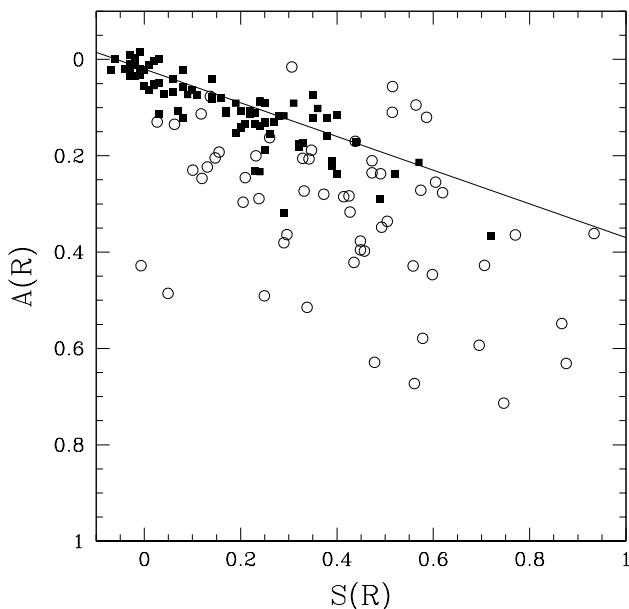


FIG. 7.— The relationship between the asymmetry, A , and clumpiness parameter, S , for the normal Frei galaxies (solid boxes) and the ULIRGs (open circles).

It has been previously argued that the asymmetry index described in §4.2 is a good and simple morphological indicator of galaxies undergoing galaxy interactions and mergers (CBJ00; Conselice et al. 2000b). The question remains, however, as to how good this structural index is at distinguishing between mergers in different stages, and how it can be used to determine if a galaxy is undergoing a minor or major merger. To answer this, we first examine the asymmetries of the 113 nearby bright normal Frei galaxies spanning all Hubble morphologies (§3.1), none of which have been involved in recent major mergers. As was shown in CBJ00, the asymmetries of the non-edge on Frei galaxies correlate with their broad-band $(B - V)$ colors (Conselice 1997; CBJ00). The asymmetries of these galaxies also correlate with the clumpiness index, S (§5.3) (see Figure 7). The fit between asymmetry and $(B - V)$ color for normal Hubble galaxies is,

$$A(R) = (-0.35 \pm 0.03) \times (B - V) + (0.35 \pm 0.03), \quad (5)$$

while the correlation between the asymmetry and the clumpiness index, S , is given by:

$$A(R) = (0.35 \pm 0.03) \times S(R) + (0.02 \pm 0.01). \quad (6)$$

The relationship between A and S for the Frei and ULIRG sample is shown in Figure 7, while the relationship between A and $(B - V)$ is discussed in detail in CBJ00. For normal galaxies that are not highly inclined, both of these correlations with A have a well defined scatter in asymmetry at various $(B - V)$ color and clumpiness (S) ranges. Figure 8 shows the difference between the Frei sample asymmetry values and the fits given in eq. (5) and (6), as a function of $(B - V)$ and S .

The average scatter in these differences for both correlations is plotted as a function of S and $(B - V)$ as open circles at two different bins, high and low S and $(B - V)$. These 1σ scatter values are roughly constant at all colors and clumpiness values, and are $\sigma(A) \sim 0.035$ for both fits.

As galaxies that are undergoing mergers appear more distorted in their stellar and gaseous distributions than a normal elliptical or spiral, the asymmetry parameter for these galaxies should intuitively increase and deviate from these fits. Indeed, this has been confirmed by studying a small number of systems undergoing mergers (Conselice et al. 2000b). Here we investigate this idea more systematically.

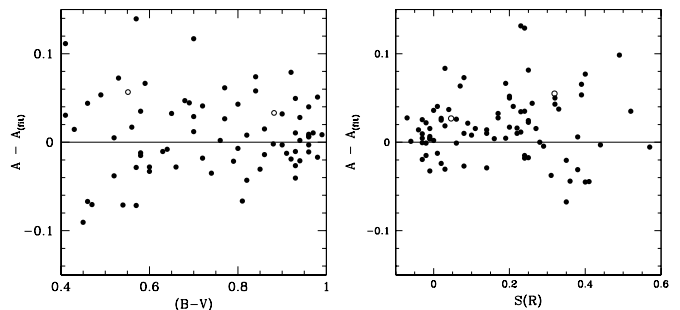


FIG. 8.— Relationship between the asymmetry deviation from the fits in eq. (5) and (6) for the Frei sample as a function of the $(B - V)$ and $S(R)$ parameter for each galaxy. The open circle is the scatter of this deviation at low and high S and $(B - V)$ values.

A merger will not in general increase the clumpiness S or color as significantly as it does the asymmetry, as galaxies that are non-interacting can be dominated by star formation as much as galaxies that are involved in a merger (e.g., Conselice 2000b; §5.3). This is supported by the starburst/merger observations presented in §3 where the S index for star-forming galaxies (starbursts and ULIRGs) are roughly the same as irregular and starburst galaxies not involved in recent mergers (§6). Furthermore, as no normal galaxies deviate significantly from the fits given in eq. (5) and (6) we argue that galaxies that deviate due to their large asymmetries, are involved in major mergers. As a limit we use $(A - A_{\text{predict}}) > 3\sigma$ from the A vs. S and A vs. $(B - V)$ correlations to identify objects that are undergoing major mergers. We test this idea below by using images of the ULIRGs, most of which are generally thought to be involved in mergers.

5.2.1. ULIRGs as Mergers

How well does the asymmetry index, as used in the CAS system, do in identifying ULIRGs as mergers? Figure 9 shows a histogram of the asymmetry values for the Frei and ULIRG galaxies. While the Frei galaxies have

mostly low asymmetries, the ULIRGs span a much larger range and include systems at all A values, including many highly asymmetric ones. Thus, the asymmetry index fails to uniquely identify all ULIRGs as mergers since many have asymmetries as low as the normal Frei galaxies. This reveals that the asymmetry index is not sensitive to all phases of the merging process, or that not all ULIRGs are mergers. Systems that have recently undergone a merger, or those in the beginning of a merger, do not have high asymmetries, as can be shown using N-body models of galaxies involved in the merger process (Conselice & Mihos in prep).

We can test the idea that the asymmetry parameter is measuring only the central phase of a major merger by plotting the IR luminosity of our ULIRG sample with the σ deviation from the asymmetry-clumpiness correlation. This comparison is shown in Figure 10 where we plot the deviation from the $A - S$ relationship (eq. 6) in units of σ deviations as a function of the ratio of the $100\mu\text{m}$ and $60\mu\text{m}$ fluxes for our ULIRG sample. Systems with the highest asymmetry values are those that have slightly higher ratios of F_{100}/F_{60} . This may demonstrate that galaxies with the highest relative $100\mu\text{m}$ fluxes have the largest asymmetries, consistent with the idea that these galaxies have heated dust from more active AGN and starbursts induced by mergers.

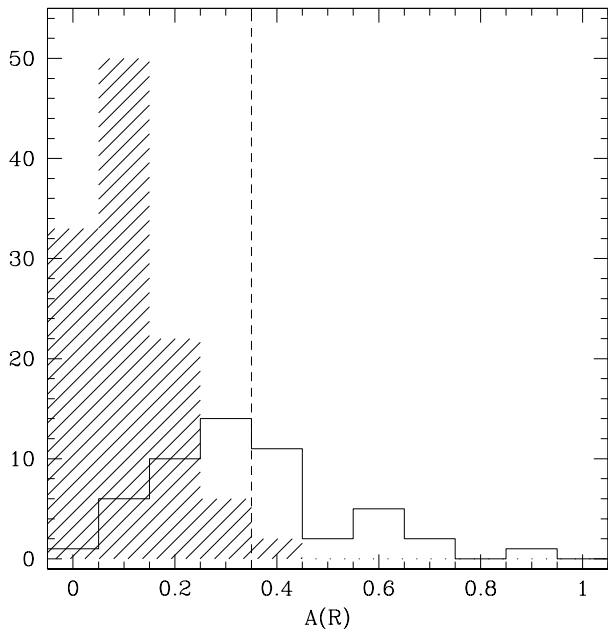


FIG. 9.— Histogram of asymmetries for the Frei galaxies (shaded) and the ULIRGs (open).

Figure 11 shows the asymmetry deviation in σ units for our ULIRGs, and Frei galaxies, from the $A - S$ correlation (Figure 7) as a function of clumpiness (S). Most systems that deviate at $> 3\sigma$ are the ULIRGs, with only a few irregulars and late-types higher than this limit. However, as mentioned earlier, not all the ULIRGs have asymmetries high enough such that they would all be identified as ongoing mergers. In fact, about 50% of the ULIRGs have asymmetries consistent with being involved in ongoing major mergers, i.e. $\delta A > 3\sigma$. This is consistent with eye-ball estimates of the fraction of ULIRGs involved in

major mergers (Borne et al. 1999). If the HST sample of 66 ULIRGs we use is representative of galaxies involved in various stages of the major merger process, then the total number of galaxies undergoing a major merger in any sample would be underestimated by a factor of two by using the asymmetry methodology.

5.3. Clumpiness - Star Formation

There is a morphological dichotomy between galaxies dominated by recent star formation and those that are not, and this is one of the major physical processes that defines the Hubble sequence, and most other galaxy morphology schemes. Traditionally, ellipticals, both normal and dwarf, have little star formation whereas spirals and irregulars often have morphologies dominated by it, especially when they are observed at ultraviolet, or optical wavelengths. For example, the morphologies of late-type spiral galaxies in optical and ultraviolet light are dominated by bright young stars (e.g., Windhorst et al. 2002). The presence, or absence, of star formation is also a fundamental parameter for understanding galaxy evolution, simply because galaxies are made of stars, and all stars were once young and therefore the passive evolution of stellar populations will have a strong effect on galaxy morphology. It is therefore desirable to find a simple method based on the appearances of galaxies that can be used to understand their star formation properties. We argue here that the clumpiness parameter is a powerful method for doing this.

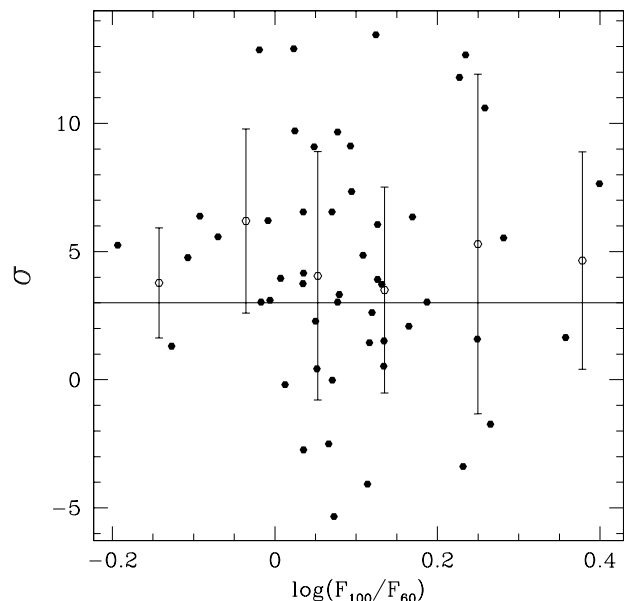


FIG. 10.— The deviation in sigma (σ) units from the asymmetry-clumpiness relationship for the ULIRGs as a function of the ratio between the IRAS flux at $100\mu\text{m}$ and $60\mu\text{m}$.

When viewing images of nearby galaxies at a fixed resolution ellipticals are the smoothest type, while spirals and irregulars have a clumpy appearance due to star clusters and stellar associations that are the sites of recent star formation. The clumpiness of a galaxy's light is partially the result of this clustering. As nearly all stars appear to form in star clusters which later dissolve (Harris et al. 2001) the idea that the clumpiness of a galaxy's light correlates with

star formation is a natural one. The best way to argue that the clumpiness parameter correlates with the presence of young stars is to determine how S traces measures of star formation, such as $H\alpha$ fluxes or integrated colors sensitive to stellar ages. Figure 12 shows the relationship between the clumpiness (S) values of the Frei galaxies and their $(B - V)$ colors taken from de Vaucouleurs et al. (1991) and their $H\alpha$ equivalent widths from Kennicutt & Kent (1983) and Romanishin (1990). From this, the clumpiness index (S) correlates with both $(B - V)$ and $H\alpha$ equivalent width, but both with a large scatter.

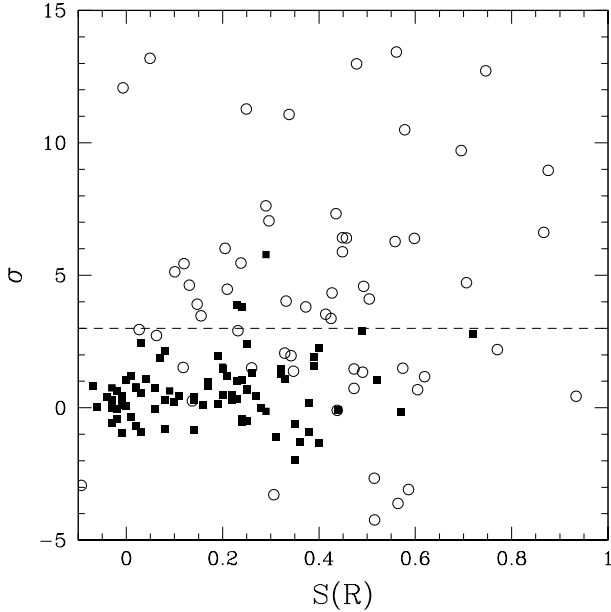


FIG. 11.— The sigma σ deviation from the the asymmetry-clumpiness relationship as a function of the clumpiness value (S) for ULIRGs (open circles) and the Frei galaxies (solid boxes).

This scatter is largely due to the effects of different viewing angles and projection effects. That is, the clumpiness parameter (S), due to its morphological nature, is sensitive to dust lanes and inclination. Figure 13 shows the residuals of the fit between $(B - V)$ and $H\alpha$ equivalent width with S , which we call δS , as a function of axis ratio, $\epsilon = \log(a/b)$ as defined in de Vaucouleurs et al. (1991). The galaxies that deviate the most from this linear fit are those with the highest inclinations, or largest axis ratios. The fit between ϵ and the scatter in the S fit, δS , can be represented as power laws

$$\delta S_{(B-V)} = (0.010 \pm 0.006) \times (1 + \epsilon)^{7.2 \pm 1.1}, \quad (7)$$

$$\delta S_{H\alpha} = (0.004 \pm 0.004) \times (1 + \epsilon)^{8.2 \pm 1.0}. \quad (8)$$

After calculating an inclination corrected S parameter by subtracting out these terms, the result of which we call $S' = S - \delta S$, we find that the correlations between S' and $(B - V)$ and $H\alpha$ significantly improves (Figure 14). The relationship between S' and $H\alpha$ equivalent width and $(B - V)$ colors is given by the best fit relationships,

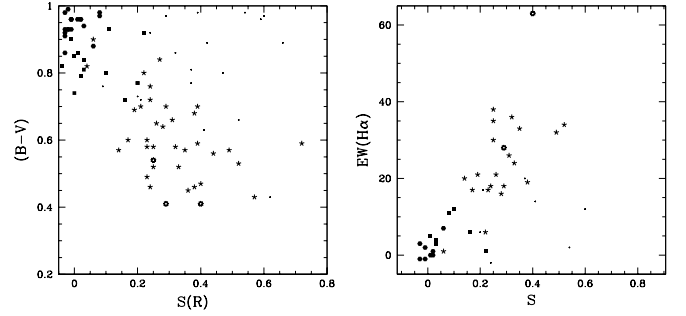


FIG. 12.— The correlation between the S parameter and $(B - V)$ color and $H\alpha$ equivalent width.

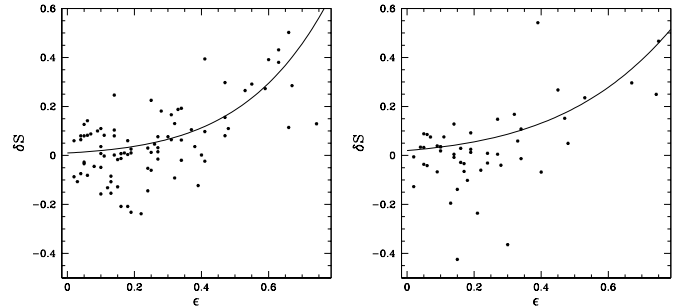


FIG. 13.— Residuals between the best fit between S and $(B - V)$ and $H\alpha$ equivalent width plotted as a function of $\epsilon = \log(a/b)$.

$$EW(H\alpha) = (82.1 \pm 10) \times S' + 3.1 \pm 2.6, \quad (9)$$

$$(B - V) = (-0.88 \pm 0.07) \times S' + 0.85 \pm 0.02. \quad (10)$$

Figure 14 shows that the inclination corrected S' parameter, measured on only a single image of a galaxy, can be used to determine, or at least place constraints on, the equivalent width of the $H\alpha$ emission from galaxies and therefore its star formation properties. This is consistent with the clumpiness parameter S as a good measure of very recent star formation as $H\alpha$ fluxes are a better measure of very young stars than broad-band colors (Gallagher, Hunter & Tutukov 1984).

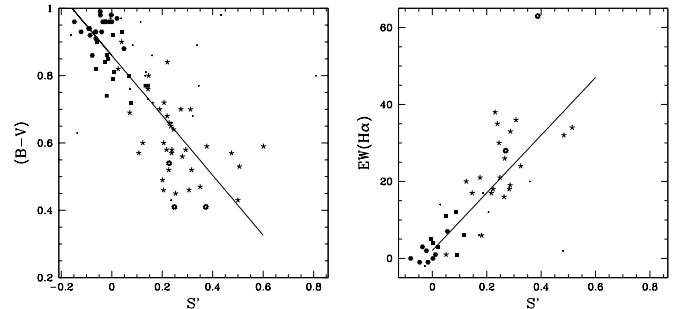


FIG. 14.— The relationship between the inclination corrected S' parameter, S' , with $(B - V)$ and $H\alpha$ equivalent width.

6. USING THE CAS SYSTEM

6.1. Locations of Galaxies in Structural Parameter Space

In this section we demonstrate that the CAS morphological parameters can be used to classify all galaxy types in a three dimensional volume. We also demonstrate how

this system can be used on high redshift galaxies. A classification cube defined by the CAS values of our sample (Tables 1 - 5) is shown in Figure 15. Each panel shows two of the structural indexes plotted against each other, while the value of the three parameter is denoted by the color of the point. The first panel shows the concentration and asymmetry indices where the color of the points give the value of the clumpiness, S , of each galaxy. Systems that have $S < 0.1$ are colored red, those with $0.1 < S < 0.35$ green, and systems with $S > 0.35$ are blue. Likewise for the $A - S$ diagram: red is for systems with $C > 4$, green for $3 < C < 4$ and blue for $C < 3$. In the $S - C$ diagram red symbols are for galaxies with $A < 0.1$, green symbols are for galaxies with $0.1 < A < 0.35$ and blue symbols for those with $A > 0.35$.

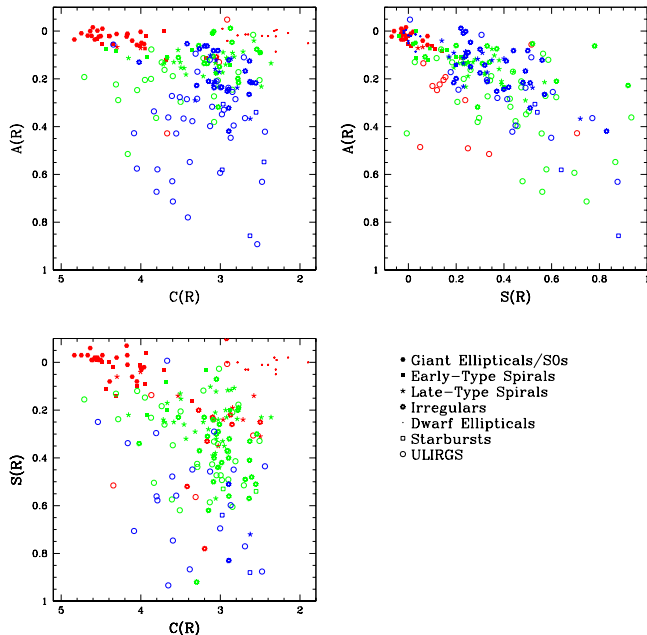


FIG. 15.— Three realizations of the different galaxy data sets plotted together by their CAS parameters. The first panel shows the concentration and asymmetry indexes plotted with colored points that reflect the value of the asymmetry for each galaxy. Systems that have clumpiness values, $S < 0.1$ are colored red, those with $0.1 < S < 0.35$ are green, and systems with $S > 0.35$ are blue. Likewise for the $A - S$ diagram: red for $C > 4$, green for $3 < C < 4$ and blue for $C < 3$ and for the $S - C$ diagram: red is for systems with $A < 0.1$, green $0.1 < A < 0.35$ and blue $A > 0.35$. This figure demonstrates that when using these three morphological parameters all known galaxy types can be distinctly separated and thus distinguished in structural space.

The average values of the concentration, asymmetry and clumpiness parameters, and their 1σ variations are listed in Table 6 for each of the broad galaxy types we study. From this table and Figure 15 all major galaxy types are cleanly separated into various regions of CAS space.

6.1.1. Ellipticals

Elliptical galaxies populate the space of high C ($\langle C \rangle = 4.4 \pm 0.3$), low A ($\langle A \rangle = 0.02 \pm 0.02$), and low S ($\langle S \rangle = 0.00 \pm 0.04$), as might be expected. A simple examination of elliptical galaxy images by eye reveals that they have very little internal structure or asymmetries. The light profiles of these systems are also fairly concentrated, something that has been known since at least Morgan (1958) and quantified by many others since then

(§5.1). The physical reasons for this are quite simple - elliptical galaxies are classified as such because they do not show evidence for recent star formation and interactions with other galaxies. Yet, because they are possibly formed from a gravitational event that removes angular momentum, or a rapid early monolithic collapse, their light is concentrated.

6.1.2. Spirals

Early-type spirals (Sa and Sb galaxies) have slightly higher asymmetries ($\langle A \rangle = 0.07 \pm 0.04$) and clumpiness values ($\langle S \rangle = 0.08 \pm 0.08$) and lower concentrations ($\langle C \rangle = 3.9 \pm 0.5$) than the ellipticals. Late-type galaxies (Sc and Sd galaxies) have even higher asymmetries ($\langle A \rangle = 0.15 \pm 0.06$) and clumpiness values ($\langle S \rangle = 0.29 \pm 0.13$) and lower light concentrations ($\langle C \rangle = 3.1 \pm 0.4$). This is also what we might have expected since spiral galaxies are known to contain modest star formation and slight asymmetries produced by star formation or minor interactions with other galaxies (CBJ00). These galaxies have lower light concentration values than the giant ellipticals because of their appreciable disks containing angular momentum.

6.1.3. Dwarf Irregulars

Dwarf irregulars have similar asymmetries as the late-type disks ($\langle A \rangle = 0.17 \pm 0.10$), but have higher clumpiness values ($\langle S \rangle = 0.40 \pm 0.20$) and lower concentrations ($\langle C \rangle = 2.9 \pm 0.3$). This is further consistent with the idea that lower-mass Hubble type galaxies are dominated by star formation. The fact that the average concentration index is low for these dwarf irregulars is also consistent with this index telling us about galaxy formation processes, and the scale of a galaxy, as these are all faint systems with $M_B < -18$ (van Zee 2000).

6.1.4. Dwarf Ellipticals

The above results are not too surprising for galaxies on the Hubble sequence whose concentration and asymmetry parameters have previously been described (e.g., CBJ00). The interesting properties of Figure 15 are for the objects considered unusual or outside the Hubble sequence that give the real power to the CAS structural indices for distinguishing galaxies in different phases of evolution.

The dwarf ellipticals in our sample have low asymmetries ($\langle A \rangle = 0.02 \pm 0.03$) and low clumpiness values ($\langle S \rangle = 0.00 \pm 0.06$), similar to the giant ellipticals (Table 6), which is probably why they were thought to be of a similar class. Yet dwarf ellipticals differ significantly from the giant ellipticals in terms of their light concentrations (Figure 15; Table 6) revealing a difference in scale, and possibly formation history, from the giant ellipticals (§5.1). The dwarf ellipticals have an average concentration value $\langle C \rangle = 2.5 \pm 0.3$, which has no overlap with the giant ellipticals, with $\langle C \rangle = 4.4 \pm 0.3$, different at a formal significance of $\sim 6\sigma$. This demonstrates the fundamental difference of scale reflected in the light concentrations of these galaxies.

6.1.5. Mergers

The interacting/merging galaxies in our sample, which includes some starbursts (SB) (Markarian 8, NGC 3690, and NGC 7673, see Table 2) and the ULIRGs (Table 5),

have on average the highest asymmetry and clumpiness values ($\langle A \rangle_{\text{SB}} = 0.53 \pm 0.22$, $\langle S \rangle_{\text{SB}} = 0.74 \pm 0.25$ and $\langle A \rangle_{\text{ULIRGs}} = 0.32 \pm 0.19$, $\langle S \rangle_{\text{ULIRGs}} = 0.50 \pm 0.40$). These are also the only galaxy types in our sample with high asymmetry and clumpiness parameters, with values larger than $S > 0.4$ and $A > 0.35$, except a few irregulars with $A > 0.35$ and a number with $S > 0.4$. This is clearly due to the active evolution occurring in these galaxies. Both starbursts and ULIRGs have intense star formation which results in high clumpiness values. Many of these galaxy types are in an active stage of a major merger, and thus have high asymmetry values, as argued earlier in Conselice et al. (2000b).

The concentration values for these two populations, is interestingly, not different from Hubble sequence galaxies with average concentrations, $\langle C \rangle_{\text{SB}} = 2.7 \pm 0.2$ and $\langle C \rangle_{\text{ULIRGs}} = 3.5 \pm 0.7$. This is consistent with violent relaxation occurring in ULIRGs, in which concentrated light profiles are established rapidly (e.g., Lynden-Bell 1967; Wright et al. 1990).

From these arguments, and the average values listed in Table 6, and individual galaxies plotted in Figure 15, we argue that galaxies in generally agreed upon different phases of galaxy evolution can be differentiated in a structural-morphological space defined by the concentration, asymmetry, and clumpiness indices. In the next section we show that the CAS parameters can be measured reliably at various S/N ratios, resolutions, and redshifts therefore making the CAS system a powerful one for understanding the evolution of galaxy populations from $z \sim 3$ until today.

6.2. Usefulness of the CAS system at High Redshift

As we are interested in applying the CAS structural parameters in future papers to decipher evolution from low to high- z , it is natural to ask how these parameters behave as galaxies become less resolved and fainter due to cosmological effects. To address this question we simulate nearby bright galaxies, used in this paper, as to how they would appear at various higher redshifts as observed in deep Hubble Space Telescope images, namely the WFPC2 and NICMOS Hubble Deep Field North and the ACS GOODS fields. After simulating these galaxies we remeasure their CAS values and compare the derived parameters to their $z \sim 0$ values. These simulations are done using the approach of Giavalisco et al. (1996), although we use a more general prescription described below.

6.2.1. Method

When simulating an image of a galaxy at z_1 to how it would appear at z_2 , with $z_2 > z_1$, several factors must be considered. The first is the re-binning factor, b , which is the reduction in apparent size of a galaxy's image when viewed at higher redshift. The other factors are the relative amounts of flux from the sky and galaxy and the noise produced from the galaxy, sky, dark current and imaging instrument (e.g., read noise). To calculate these, we generalize the procedure for simulating a hypothetical galaxy with actual size d (measured in kpc, for example) imaged at a redshift z_1 which we want to simulate at z_2 . At a given higher redshift z_2 this galaxy will subtend an angle,

$$\theta_{z_2} = \frac{d}{A_{z_2}} = d \frac{(1+z_2)^2}{L_{z_2}}, \quad (11)$$

where A_z is the angular diameter distance, which is related to the luminosity distance (L_z) by $A_z = L_z/(1+z)^2$. The number of pixels in a galaxy, as imaged at a redshift z , is given by $n_z = \theta_z/s_z$ where s_z is the angular size of the pixels used in the detector to image the galaxy at redshift z . At the redshift z_2 the galaxy will subtend an angle θ_{z_2} which will appear on the simulated image with a size in pixels n_{z_1}/n_{z_2} times smaller than the original image with an angular size θ_{z_1} . The ratio of these galaxy sizes in pixel units is the binning factor (b) which can be written as

$$b = n_{z_1}/n_{z_2} = \frac{\theta_{z_1} s_{z_2}}{\theta_{z_2} s_{z_1}} = \frac{(1+z_1)^2 L_{z_2} s_{z_2}}{(1+z_2)^2 L_{z_1} s_{z_1}}. \quad (12)$$

The luminosity distance, L_z can be expressed as an analytic formula for cosmologies with $\Omega_\lambda = 0$ (Giavalisco et al. 1996), but for the cosmology used here, $\Omega_\lambda = 0.7$, $\Omega_m = 0.3$, L_z must be computed numerically (e.g., Peebles 1980). The amount the observed galaxy must be reduced in surface brightness is computed by using the conservation of energy, that is the luminosity before and after reshifting is the same, or

$$4\pi\alpha_{z_1} N_{z_1} p_{z_1} L_{z_1}^2 (1+z_1) = 4\pi\alpha_{z_2} N_{z_2} p_{z_2} L_{z_2}^2 (1+z_2) \frac{\Delta\lambda_{z_1}}{\Delta\lambda_{z_2}}, \quad (13)$$

for a galaxy observed in filters at central rest frame wavelengths λ_{z_1} and λ_{z_2} and filter widths of $\Delta\lambda_{z_1}$ and $\Delta\lambda_{z_2}$. N_z is the total number of pixels covering a galaxy at z and p_z is the average ADU s^{-1} per pixel. The calibration constant α_z is in units of $\text{erg s}^{-1} \text{cm}^{-2} \text{\AA}^{-1}$ (ADU s^{-1}) $^{-1}$. Since $N_z \sim (\theta_z/s_z)^2$ and by using eq. (12) we can rewrite eq. (13) in terms of p_{z_2} in ADU counts as

$$p_{z_2} = p_{z_1} \frac{\alpha_{z_1}}{\alpha_{z_2}} \left(\frac{s_{z_2}}{s_{z_1}} \right)^2 \left(\frac{1+z_1}{1+z_2} \right)^4 \frac{\Delta\lambda_{z_2} t_{z_2}}{\Delta\lambda_{z_1} t_{z_1}} \quad (14)$$

where t_z is the respective exposure times at the observed redshift z_1 and simulated higher redshift z_2 . An extra factor of $(1+z_2)/(1+z_1)$ has been applied to eq. (14) to account for the smaller rest-frame wavelength observed at z_1 than at z_2 . The observed flux of the simulated galaxy as seen at z_2 in ADU units can be computed through the use of eq. (14). Note that ideally we minimize k-corrections in this approach by matching the observed wavelengths at z_1 and z_2 .

The sky background is then added to these images by the addition of $B_z \times t_z$, where B_z is the amount of light from the background in units of ADU s^{-1} . Note that the original background in the z_1 image has already been removed prior to artificially redshifting. Noise components are then added in, which include: read-noise scaled for the number of read-outs, dark current and photon noise from the background. Finally the resulting image is smoothed by a PSF appropriate for various HST instruments as generated by Tiny-Tim (Kriss et al. 2001).

To understand how well we can measure the CAS parameters at high redshift we simulated various galaxies

in our sample out to redshifts of $z = 3$ using the above approach. As we use rest-frame optical images we implicitly assume a zero morphological k -correction. Although galaxies clearly appear different in the rest frame optical and ultraviolet (e.g., Windhorst et al. 2002; cf. Conselice et al. 2002c for starbursts) we want to isolate the effects of decreased resolution, and increased noise, on the CAS parameters so therefore use the same image.

To understand and quantify how well the CAS parameters can be measured at high redshifts we carried out three different simulations. Two of the simulations consisted of placing the Frei sample at redshifts from $z \sim 0.5$ to 3 as they would appear in the Hubble Deep Field WFPC2 F814W (I) and the GOODS F850L (z) images. We then measure the CAS values on these simulated images to determine how they have changed.

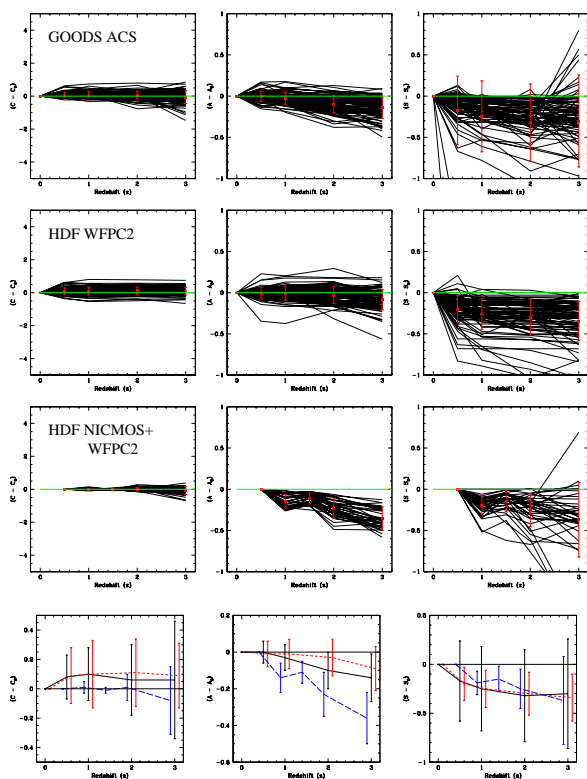


FIG. 16.— Determination of redshift effects on the measurement of the CAS parameters. In the top two panels (a and b) the 82 galaxies that comprise the Lowell Frei sample (see Frei et al. 1996; Conselice et al. 2000a) are simulated to how they would appear at $z = 0.5, 1, 2$ and 3 in (a) the GOODS ACS F850L (z) imaging and (b) the F814W (I) image of the Hubble Deep Field North. The third panel (c) shows how the 38 galaxies with $M_B < -18$ in the Hubble Deep Field North would appear at higher redshifts in the rest-frame B-band. This is done by using the WFPC2 + NICMOS images of the Hubble Deep Field North, which allows the rest-frame appearance of galaxies to be seen out to $z \sim 2.5$. We simulate this $z \sim 0.5$ sample to $z = 1, 1.5, 2$ and 3. The numbers plotted are with reference to the $z \sim 0$ (or $z \sim 0.5$ value for NICMOS) CAS parameters (C_0, A_0, S_0). The green line shows the zero level and the red dot and errorbars are the averages and 1σ variations at each simulated redshift. The bottom panel shows the average differences and their 1σ scatter values for the GOODS (solid dark line), HDF WFPC2 (red dashed line) and the NICMOS+WFPC2 simulations (long blue dashed line).

We also performed a simulation accounting for morpho-

logical k -corrections by simulating galaxies with $M_B < -18$ found in the Hubble Deep Field North between $0.4 < z < 0.7$ to higher redshifts. At $z \sim 1.2$ the rest-frame B-band morphologies of these galaxies are sampled in the observed NIR, thus we carry out simulations using the WFPC2 images for these galaxies at $z < 1.2$ and the NICMOS HDF-N observational parameters in the F110W and F160W bands (Dickinson et al. 1998) at $z > 1.2$.

6.2.2. GOODS ACS Fields

The GOODS fields consist of deep BViz imaging in the Hubble Deep Field North and Chandra Deep Field South regions taken as part of the initial ACS Treasury program (see <http://www.stsci.edu/ftp/science/goods/>). For our simulations we use the observing parameters for the F850L (z-band) observations (Giavalisco et al. 2003 in prep). Our simulated images therefore match the conditions in which these galaxies are observed, sans morphological k -corrections as we use the rest-frame B-band image of each galaxy in the simulation. After simulating the 82 Lowell Frei galaxies as to how they would appear in the z-band image of ACS GOODS, we run the CAS program on each system. This is first done by remeasuring the $1.5 \times (\eta = 0.2)$ radii, and then measuring the CAS parameters within this. We do not assume a radius for each galaxy, but remeasure everything as if it were a new galaxy, with unknown $z = 0$ properties.

The three panels in Figure 16a show how the concentration index C , asymmetry index A , and clumpiness index, S , change for each of the 82 galaxies as a function of redshift with respect to their $z = 0$ values, with $z = 0.5, 1, 2$, and 3 simulated as described above. The average differences from $z = 0$ and their 1σ deviations are plotted as red dots and error-bars, and are listed in Table 7. In Figure 16d the average differences for the GOODS CAS parameters and their 1σ variations are plotted as the solid dark line.

6.2.3. WFPC2 Hubble Deep Field North

We perform a similar simulation as done for the GOODS z-band field, but using the observing parameters in which the WFPC2 F814W Hubble Deep Field observations were acquired (see Williams et al. 1996). The results of these simulations are shown in Figure 16b, and are plotted in Figure 16d as the dashed red line. The same procedure described in §6.2.2 is also used to simulate these galaxies.

6.2.4. NICMOS+WFPC2 HDF - Eliminating the Morphological k -correction

By simulating galaxies into the NICMOS images of the Hubble Deep Field North taken by Dickinson et al. (1998), combined with matched seeing WFPC2 images from Williams et al. (1996) we can determine the rest-frame morphological appearance of galaxies from $z = 0$ to ~ 2.5 . This eliminates the morphological k -correction, as the NICMOS F110W ($1.1 \mu\text{m}$) and F160W ($1.6 \mu\text{m}$) bands allow us to sample rest-frame B-band morphologies out to $z \sim 2.5$. From this we can determine how morphological indices are changing purely as a function of redshift, without worrying about band shifting effects. A more detailed analysis of this problem is presented in Conselice et al. (2003b). We carried out this simulation by using low redshift galaxies in the HDF, and simulating them to higher

redshifts. For this, we used the 38 galaxies with $M_B < -18$ at redshifts $0.4 < z < 0.7$ found in the HDF North. The result of these simulations are shown in Figure 16c when simulating the $z \sim 0.5$ galaxies to $z = 1, 1.5, 2$ and 3 . The average CAS value differences between the values at $z \sim 0.5$ and the higher redshifts are shown in Figure 16d as a blue line.

6.2.5. Simulation Results

From these diagrams it is clear that at least the asymmetry and concentration indices are reproducible out to $z = 3$, within a reasonable scatter. This is especially the case when using the average differences for a given population, as it is nearly zero, or can be corrected to zero, for galaxies at any redshift, the possible exception being the NICMOS observations which have a lower resolution than the WFPC2 or ACS data.

The asymmetry and clumpiness spatial indices also decline, on average, as a function of redshift while the concentration index slightly increases from a zero difference as a function of redshift. From Figure 16 it is clear that one cannot be certain after measuring CAS parameters on a single high redshift galaxy what its $z \sim 0$ value would be. The average CAS values of a given population can however be corrected to a statically average $z \sim 0$ value which can be used for comparing evolution. The CAS values of a single galaxy at $z > 1$ will, on average, have an uncertainty that will make their use somewhat limited until deeper high resolution imaging is carried out.

These simulations are also generally idealized and do not include the improved image quality and effective resolution produced by drizzling. The average differences and their 1σ scatter also improve when only considering very bright galaxies, or those with active star formation. A detailed analysis of this, and how CAS values for different galaxy populations change with redshift in these simulations is however beyond the scope this paper, but will be address fully in future studies of high redshift systems.

7. SUMMARY

One of the major problems in extragalactic astronomy is the absence of a well defined physical classification system for galaxies. Ideal classification systems are those that classify objects according to their most salient physical or evolutionary properties and processes. In this paper we introduce a model independent morphological system that measures fundamental formation processes and their past history and uses these features to classify all galaxies. This is done by using the concentration index (C), the asymmetry parameter (A) and a clumpiness index (S).

The concentration index reveals how concentrated a galaxy's light is, while the asymmetry index and clumpiness indices quantify how disturbed and clumpy light distributions are. We argue in this paper that the concentration index is a measure of the relative fraction of light in bulge and disk components, i.e., the B/T ratio, and is a measure of the scale of a galaxy - its size, luminosity and mass. Concentration thus reveals the past formation history of a galaxy. The asymmetry index is shown to be good at identifying galaxies which are currently undergoing major mergers. The clumpiness index is found to correlate very well with the $H\alpha$ equivalent width of galaxies, and to a lesser degree with the integrated ($B - V$)

color of a galaxy.

After constructing a volume out of the CAS parameters for 240 nearby galaxies in all phases of evolution, we find that all major nearby galaxy types (ellipticals, late and early-type spirals, irregulars, starbursts, mergers, and dwarf ellipticals) can be cleanly distinguished from each other automatically and computationally. We also demonstrate that this classification system can be applied at high redshift by showing that average CAS parameters can be accurately determined for any galaxy population seen in deep Hubble Space Telescope images out to $z \sim 3$. As the Advanced Camera for Surveys will provide an unprecedented morphological view of high redshift galaxies, we hope that the CAS system will be useful for understanding and determining how galaxy evolution and formation has occurred.

I thank my collaborators, especially Richard Ellis, Matt Bershad, Mark Dickinson, Jay Gallagher and Rosie Wyse whose work with me led to the present ideas and paper. Richard Ellis, Andrew Benson, Matt Bershad, Tommaso Treu, and an anonymous referee made valuable suggestions after reading various versions of this paper. I also thank Eric Peng for allowing me to use his GALFIT program. This work was supported by a National Science Foundation Astronomy and Astrophysics Fellowship and by NASA HST Archival Researcher grant HST-AR-09533.04-A, both to CJC.

APPENDIX

DECONSTRUCTING THE HUBBLE SEQUENCE

The Hubble morphological system has been the dominate galaxy classification paradigm since its first publication in 1926³ (Hubble 1926). The basic tuning-fork morphological system was later expanded and revised (Hubble 1936; Sandage 1961; de Vaucouleurs 1959; van den Bergh 1960) to include additional galaxies such as the Sd and S0 types as well as morphological features such as rings, ‘S’ shapes, and other features. These later morphological properties however add little to the physical meaning of a ‘morphological-type’ and are rarely used in practice except for very specific purposes.

Despite the wide acceptance of the Hubble system, there are many well know problems with it, for example see van den Bergh (1998), Conselice et al. (2000a), van den Bergh, Cohen & Crabbe (2001), and Abraham & van den Bergh (2001) for discussions of this problem. One major issue is that at redshifts higher than $z \sim 1$ the Hubble sequence no longer provides a useful frame-work for understanding galaxies (van den Bergh et al. 2001). Not only is it difficult, to impossible, to accurately obtain a Hubble type from an algorithm (Naim et al. 1995a; Odewahn et al. 2002) but classification experts often do not agree among themselves on subjective classifications (Naim et al. 1995b). The result of this is that the physical meaning of a Hubble type is unclear (e.g., Roberts & Haynes 1988) as a Hubble type does not alone uniquely reveal any physical property. That is, the Hubble classification system does not identify, or distinguish between, galaxies involved in very different modes of evolution, except for the basic trichotomy between ellipticals, spirals, and irregulars which vary significantly between each other in most measurable properties.

Hubble classifications are also internally inconsistent within its own classification requirements. This can be seen by investigating the criteria for classification into different Hubble types. According to Sandage (1975), the criteria for classification on the Hubble sequence relies on three subjective properties: “(1) the size of the nuclear bulge relative to the flattened disk, (2) the character of the spiral arms, and (3) the degree of resolution into stars and HII regions of the arms and/or disk.” This is similar to the original criteria used by Hubble (1926) 50 years earlier: “(1) relative size of the the unresolved nuclear region; (2) extent to which the arms are unwound; (3) degree of resolution in the arms.” Criterion (3) is entirely insufficient for comparing galaxies, since the degree of resolution depends strongly on distance, telescope resolving power and seeing, and we argue has rarely been a real criteria for placing galaxies on the Hubble sequence (cf. Sandage & Tammann 1981). Criterion (2) relates to the pitch angle of spiral arms from the nuclear or bulge region, and to the presence of strong bars in spirals, while criterion (1) is the relationship between spiral bulge and disk sizes.

Since criteria (3) is a largely inadequate for classifying galaxies at different resolutions let us examine the other two conditions to determine how well they correlate. To answer this question, Kennicutt (1981) measured the pitch angles (ψ) of 113 spiral galaxies to determine how ψ values correlate with Hubble types as classified in the Revised Shapley-Ames Catalog (Sandage & Tammann 1981). As shown by Kennicutt (1981) there is only a weak correlation between the Hubble type and pitch angle of spiral arms. We can reexamine Kennicutt’s (1981) data to determine how well pitch angles correlate with T-types as determined by de Vaucouleurs et al. (1993) where each spiral T-type is based on the Sandage (1961) criteria. Figure 17 shows this comparison. Although on average pitch angles increase for latter T-types, the 1σ variations of the average ψ for each T-type clearly overlap for galaxies later than, and including, Sbs. This is an indication that the methodology for classifying Hubble types is not sound, as the criteria is neither internally consistent, nor, as discussed above, does it reveal unique galaxy populations. As such, classifiers using the Hubble sequence often must pick either estimating the bulge to disk ratio, or the pitch angle of spiral arms, to place a galaxy into a type, as has been recognized for many years (e.g., Sandage 1975).

Furthermore, recent results show that the ratio of bulge and disk sizes is scale free along the Hubble Sequence (e.g., de Jong 1996; Coureau, de Jong & Broeils 1996); that is, the ratio of bulge to disk scale lengths is roughly constant for different spiral Hubble types. It is also often assumed that the Hubble sequence correlates with physical features, such as stellar populations, colors and star formation histories, since the work of Holmberg (1958). As for pitch angles, this is true for Hubble types in the mean, but there is a large scatter of physical properties at every Hubble stage (e.g., Roberts & Haynes 1994; Kennicutt 1998). There is also evidence that all spiral Hubble classes have roughly the same average star formation properties (e.g., Devereux & Hameed 1997; Hameed & Devereux 1999). Therefore, a basic Hubble type does not reveal any fundamental physical information about a particular galaxy, and in practice a Hubble type is often used only as a guide for understanding a galaxy rather than as a useful physical description. This is the result of the most prominent features of galaxies being not necessarily useful for determining the physical evolution of a galaxy, as we argue below.

Bars, Rings and Spiral Arms

Galaxy bars are very visible, and as such, have been a major classification component since the work of Curtis (1918). Hubble (1926) made the distinction between barred and unbarred spirals the major division in spiral galaxies, and bars put the ‘fork’ in the Hubble tuning fork. De Vaucouleurs (1959) considered bars important enough that his classification system uses weak or strong bars as a fundamental criterion.

Although the classification of spiral galaxies into barred and unbarred is often done, it is important to ask if this is a useful feature for understanding galaxies and their evolution. Many disk galaxies, if not most, have some kind of central

³Hubble (1926) was the first to set forth the systematic classification system that now bears his name, although early photographic work on galaxies revealed that spiral galaxies come into many forms, including the barred or ϕ classification (Curtis 1918). Several other galaxy classification systems predate Hubble’s, such as Wolf’s (1908) rich descriptive taxonomy, although these classification were not generally in use after 1945 (Sandage 1975).

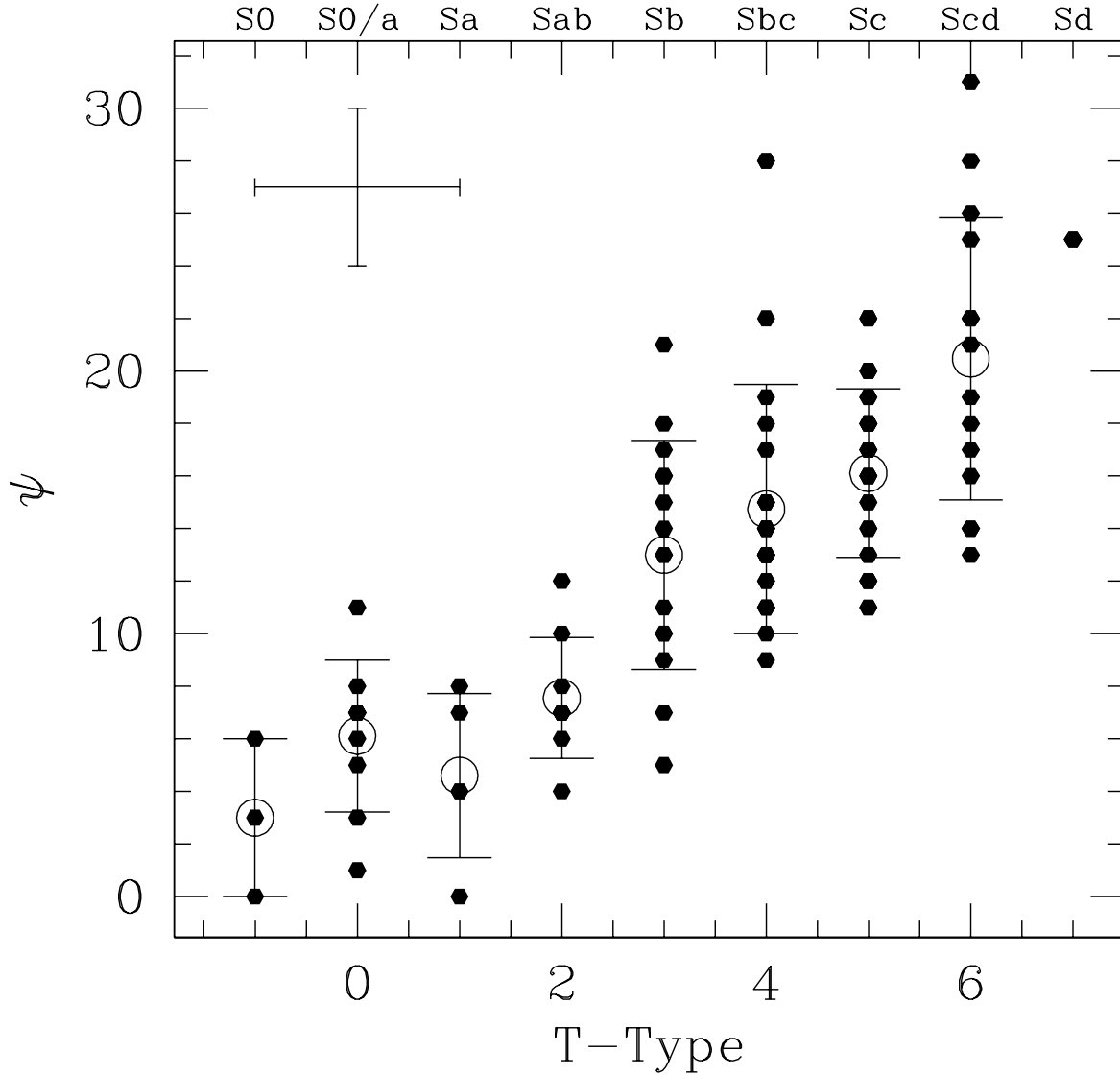


FIG. A17.— The pitch angle ψ for spiral galaxies, as measured by Kennicutt (1981), plotted against Hubble type estimates as determined by de Vaucouleurs et al. (1993). The open circle denotes the average pitch angle at each T-type and the plotted error is the 1σ variation. There is no statistically significant difference between the measured pitch angle for galaxies classified as Sb (T=3) or later.

bar (Buta & Combes 1996). This is especially true when examining galaxies at red wavelengths (e.g., Eskridge et al. 2000) where the bar fraction can be over 60% in the near infrared. Galaxies with or without bars do not differ significantly in terms of physical features such as stellar populations (de Vaucouleurs 1961) which suggests that bars cannot be a fundamental feature, in themselves. Bars are not seen in other galaxy types such as ellipticals and therefore are only properties of disks. In principle, bars can also form and reform without changing the basic evolution of a galaxy. They are still important however as they trace the effects, and are the causes of evolutionary phenomenon, such as interactions and star formation.

The rings and s-shaped patterns popular in the de Vaucouleurs (1959) revision of the Hubble Sequence and used by Sandage (1961) and others, are related to bars in some way and are also not salient classification features for similar reasons. Rings are useful for identifying the locations of resonances in galaxies (Buta & Combes 1996), and again are likely transient in nature. There are also no obvious physical differences between galaxies that have bars and rings and those that do not (van den Bergh 1998). Rings can, like bars, also harbor star formation (Buta & Combes 1996) and are likely related to bars and spiral arms (e.g., Buta & Combes 1996).

Like bars and rings, spiral patterns are a transient phenomenon and trace the location of galactic disks. They are also probably the most spectacular morphological feature in galaxies and are the principle feature of the Hubble sequence. As traditionally observed at optical wavelengths, most spiral arms contain bright young stars that only account for a very small fraction of a galaxy's mass. Spiral arms also look very different when observed at various wavelengths, as first discussed by Zwicky (1957). At shorter wavelengths, particularly in the near infrared, pitch angles decrease and nuclear regions increase in relative size, changing the Hubble type. The near infrared is in fact a better place to study stars in galaxies since a better idea of the true mass distribution is obtained (e.g., Block & Puerari 1999). The fact that bulge to disk ratios, pitch angles, and spiral arm structure changes with wavelength is also a hint that the properties of spiral arms are not ideal criteria for classifying galaxies. In summary, bars, rings and spiral arms are all features that signify internal dynamics of disk galaxies, but they alone are not fundamental evolutionary changes in a galaxy, and therefore should not be used to physically classify galaxies.

THEORETICAL CLASSIFICATION

Galaxy evolution can be understood through the use of stellar structures in a variety of models, such as in the hierarchical context or monolithic collapse, by the simple use of scaling relationships between quantities and observables, and an understanding of the various components and evolutionary processes occurring in galaxies. To demonstrate this we start by writing the mass of a galaxy as a function of time, $M_T(t)$, as a composition of stars, gas and dark matter as,

$$M_T(t) = M_S(t) + M_G(t) + M_{DM}(t), \quad (\text{B1})$$

where $M_S(t)$, $M_G(t)$ and $M_{DM}(t)$ are the stellar, gaseous and dark matter mass of a galaxy at a given time, t . In the CDM scenario, at $t_0=0$ when the dark matter halo first collapses, $M_S(t_0) = 0$. Over time, star formation occurs and various forms of mass will be accreted and removed from a galaxy due to interactions and mergers, changing the composition, and quantity, of a galaxy's mass. At a time $T > t_0$, the total amount of mass added to, or removed from, a galaxy by interactions, mergers and accretion, $\delta M_T(T)$ is given by,

$$\delta M_T(T) = \delta M_S(T) + \delta M_G(T) + \delta M_{DM}(T) = \int_0^T \dot{M}_T(t) dt = \int_0^T \dot{M}_S(t) dt + \int_0^T \dot{M}_G(t) dt + \int_0^T \dot{M}_{DM}(t) dt, \quad (\text{B2})$$

where $\dot{M}_T(t)$ is the mass accretion or removal rate in units of $M_\odot \text{ time}^{-1}$, and T is the age of the galaxy when observed. We further divide the mass flux into stellar $\dot{M}_S(t)$, gaseous $\dot{M}_G(t)$ and dark matter $\dot{M}_{DM}(t)$ components.

In this scenario gas will be obtained by two methods, in addition to any gas present at initial formation ($M_{G,0}$). Gas can be obtained through gravitational processes such as mergers⁴, $\delta M_{G,G}(t)$, and from gas accreted smoothly over time through deposition, $\delta M_{G,D}(t)$. We can then write the addition of a galaxy's gas mass as two components, such that $\delta M_G = \delta M_{G,G} + \delta M_{G,D}$. The total gas mass can be written as, $M_G(t) = M_{G,G}(t) + M_{G,D}(t) + M_{G,0}(t)$. Gas in a galaxy will be converted into stars as a function of time, t , by a conversion rate, $\alpha(t)$, defined as the fraction of gas mass converted into stars per unit time, such that the star formation, $\delta M_{G \rightarrow S}$, is given by

$$\delta M_{G \rightarrow S}(T) = \int_0^T \alpha(t) M_G(t) dt = \int_0^T \alpha(t) (M_{G,G}(t) + M_{G,D}(t) + M_{G,0}(t)) dt = \delta M_{S,G}(T) + \delta M_{S,D}(T) + \delta M_{S,0}(T), \quad (\text{B3})$$

where $M_G(t)$ is the total gas mass as a function of time, and $M_{G,G}$, $M_{G,D}$ and $M_{G,0}$ are the gas masses of a galaxy obtained from through the gravitational process of mergers, gas deposited from accretion, and the original gas present.

The stellar mass of a galaxy, $M_S(t)$, is therefore formed from gas placed into a galaxy by several physical methods. It could have formed through smooth gas deposition ($M_{S,D}$), gravitational collapse (i.e., mergers) of existing stars ($M_{S,G}$),

⁴In this instance mergers implies that the gas is brought into a galaxy in discrete units, such as attached to an existing galaxy or dark matter halo. This is opposite to gas accreted from the intergalactic medium which is not necessarily added to the galaxy in discrete units, but is added smoothly over time.

or conversion from the original gas in the galaxy, $M_{S,0}$, such that $M_S(t) = M_{S,G}(t) + M_{S,D}(t) + M_{S,0}(t)$. More generally, we can write the total stellar, gas, and dark matter masses of a galaxy as a function of time as

$$M_S(T) = \int_0^T \left(\dot{M}_S(t) + \alpha(t)M_G(t) \right) dt, \quad (\text{B4})$$

$$M_G(T) = M_{G,0} + \int_0^T \left(\dot{M}_G(t) - \alpha(t)M_G(t) \right) dt, \quad (\text{B5})$$

$$M_{DM}(T) = M_{DM,0} + \int_0^T \left(\dot{M}_{DM}(t) \right) dt. \quad (\text{B6})$$

Where the total mass of a galaxy at a given time is given by equation B1. Equation B6 assumes that the dark matter in a galaxy is non-baryonic, or at least cannot be converted into stars. We also do not account here for stellar feedback into the intergalactic medium, which would include a term in eq. B5 to account for supernova material and other mass ejecta from stars, but this can be easily done (e.g., Sandage 1986).

Most of the original stellar mass in galaxies probably formed from an initial deposition of gas, thus $M_S(t_{\text{gal}}) = M_{S,D}(t_{\text{gal}})$ where t_{gal} is the time when the first generation of stars formed. Later, through mergers and star formation processes, the total stellar mass of a galaxy will increase and stellar mass will be redistributed through gravitational processes, if mergers occur, while new stars are formed from gas deposition and gas obtained through mergers. We can relate the time variable ratio of mass created through these various methods by the parameter $D(T)$, defined as the fraction of stellar mass formed through gravitational processes:

$$D(T) = \frac{M_{S,G}(T)}{M_S(T)} = \frac{\int_0^T \left(\dot{M}_S(t) + \alpha(t)M_{G,G}(t) \right) dt}{\int_0^T \alpha(t)M_G(t)dt}. \quad (\text{B7})$$

This fraction can then be used, knowing the value of $D(T)$, to track the gross morphological evolution of a galaxy's stellar and how it is globally distributed.

In principle the CAS parameters can be represented by three observable terms in equations B1 - B7. Light concentration, which is the fraction of stars produced through gas depositionally placed, can be represented by $D(T)$, which does not change with time unless star formation, accretion, or mergers occur. The asymmetry parameter can be represented by $M_{S,G}(t)$ and the clumpiness, S , which is a measure of star formation, can likewise be represented by $\delta M_{G \rightarrow S}(t)$ (eq. B3).

Understanding the correspondence between these theoretical quantities and measurable properties requires a very good knowledge of the internal evolution of galaxies, including stellar evolution and dynamical relaxation processes and their related time scales. We can however create other dimensionless parameters, similar to B7, that in principal directly correlate with the asymmetry and clumpiness, indicating the evolutionary state of a galaxy. As this paper is focused on answering the question of whether or not we can use stellar light to measure these properties, the integrated deposition $D(T)$ (eq. B7), star formation $F(T)$ and interaction, $I(T)$ features weighted by mass and time can be written in terms of measurable dimensionless indices as:

$$F(T) = \int_0^T \frac{t}{T} \frac{\alpha(t)M_G(t)}{M_S(T)} dt. \quad (\text{B8})$$

$$I(T) = \int_0^T \frac{t}{T} \frac{|\dot{M}_S(t)|}{M_S(T)} dt \quad (\text{B9})$$

These three parameters (eq. B7 - B9) are dimensionless physical morphological quantities that correlate with the stellar appearance of a galaxy and fundamental evolutionary processes, such that $C \propto D$, $A \propto I$, and $S \propto F$. Equations (B8) and (B9) are weighted by time since older star formation and interactions will have less of an effect on the appearance of a galaxy. Likewise, galaxies with higher stellar masses will have appearances that in general are less effected by star formation, and stars lost or gained from galaxy interactions. The parameter $D(T)$ can of course change, but it is not an integral of time since the amount of stellar mass settled by depositional or gravitational processes does not passively evolve without outside influences. Star formation in a galaxy, or interactions between galaxies however does morphologically evolve in a few Gyrs (i.e., stellar aging, cluster dissolution and relaxation processes smooth out effects from star formation and galaxy interactions).

Predicting Structural Features

By using equations (B7) through (B9), it is possible to investigate the theoretical evolution a galaxy's structure. This requires understanding some basic physical features such as the fraction of gas mass converted into stars per unit time, $\alpha(t)$, and the history of interactions with other galaxies.

There are many ways to investigate simple cases of theoretical morphology and its evolution, only a few of which we examine here. A simple case is to assume that a galaxy contains an initial amount of gas that declines exponentially at

a constant scale-factor, α , due to star formation. This gas mass is converted into stellar mass, thereby producing star formation that will induce morphological changes into the system under study. Solving equation (B5) using a constant α , with no new additions of gas, gives an exponential decrease in the gas mass,

$$M_G(t) = M_{G,0} \times \exp(-\alpha t). \quad (\text{B10})$$

By using eq. (B10) with eq. (B8), the index $F(t)$ can be written in this situation as,

$$F(T) = \frac{M_{G,0}}{T \times M_S(T)\alpha} \times (1 - \exp(-\alpha T) \times (\alpha T + 1)). \quad (\text{B11})$$

The evolution of the $F(T)$ parameter as a function of redshift in this scenario is plotted in Figure 18a and b for a $\Omega = 1$ universe. Figure 18a shows seven different curves for various values of α from 0.3 for the highest curve, to $\alpha = 0.9$ for the curve with the lowest values at the higher redshifts. Figure 18b shows $F(t)$, as a function of redshift, when α is held constant at 0.2, while allowing the ratio $M_{0,G}/M_S$ to vary from 1 to 0.4. We can likewise write the interaction parameter, $I(t)$, in a similar way, assuming that the amount of mass gained or lost declines exponentially with time such that $|\dot{M}_S(t)| = |\dot{M}_0| \times \exp(-\beta t)$, as

$$I(T) = \frac{|\dot{M}_0|}{T \times M_S(T)\beta^2} \times (1 - \exp(-\beta T) \times (\beta T + 1)). \quad (\text{B12})$$

Figure 19 plots $I(T)$ in this form, where the parameter β is varied between 0.1 - 0.7. Figure 19b shows $I(T)$ when varying the ratio of $|\dot{M}_0|/M_S(T)$. Both Figure 18 and 19 demonstrate that if galaxies have exponentially declining star formation and interaction histories then their morphologies are dominated by these effects at redshifts from $z = 1$ to 3. This is broadly consistent with observations that show galaxies in this redshift range have blue colors and high star formation rates (e.g., Ellis 1997).

Another simple star formation and galaxy interaction scenario that can be investigated is when the amount of gas available for star formation, M_G , and mass removal/addition rate, $|\dot{M}_S(t)|$ and α , are constant as a function of time. This would be the case in the situation where instantaneous recycling of gas occurs after star formation, or gas is continuously accreted onto a galaxy. In these cases, the parameters $F(T)$ and $I(T)$ reduce to,

$$F(T) = \frac{T \alpha \times M_G}{2 M_S(T)}, \quad (\text{B13})$$

$$I(T) = \frac{T |\dot{M}_S|}{2 M_S(T)}, \quad (\text{B14})$$

the forms of which are plotted in Figure 18c and 19c for the same seven ratios of $M_{G,0}/M_S$ and $|\dot{M}_S|/M_S(T)$ used in Figure 18b and 19b.

The third and final form we investigate are star formation and interaction events occurring in random ‘bursts’ during galaxy evolution. Figure 18d and 19d show the result of this scenario, where the spikes are at the redshifts when star formation and mergers occur for 10 Myrs, and then turn off. We can solve for both $F(t)$ and $I(t)$ when both star formation and interactions occur at these discrete times. The form of these equations are,

$$F(T) = \frac{\alpha}{T \times M_S(T)} \sum_{i=0}^N t_i \times M_G(t)_i \Delta T_i, \quad (\text{B15})$$

$$I(T) = \frac{1}{T \times M_S(T)} \sum_{i=0}^N t_i \times |\dot{M}_S(t)_i| \Delta T_i, \quad (\text{B16})$$

where N is the number of star burst or merger events, t_i is the time when each event occurs, and ΔT_i is the time duration of each event. These simple scenarios are meant to show that if we knew the detailed interaction and star formation history of each galaxy, we could use eqs. (B7 - B9) to calculate its gross morphological appearance, and the theoretical values of C , A and S , as a function of redshift.

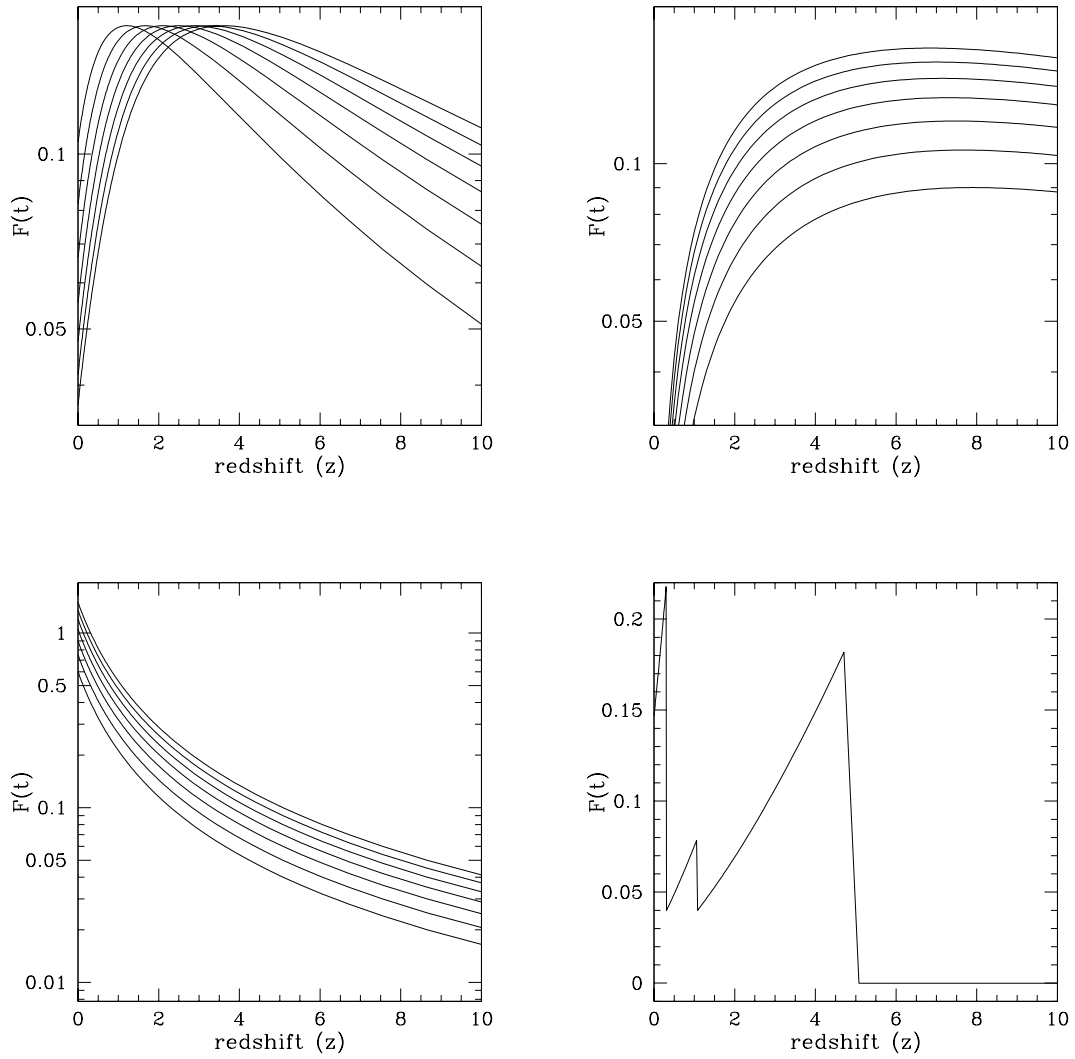


FIG. B18.— How the F parameter is predicted to change as a function of redshift in different galaxy evolution scenarios (see text).

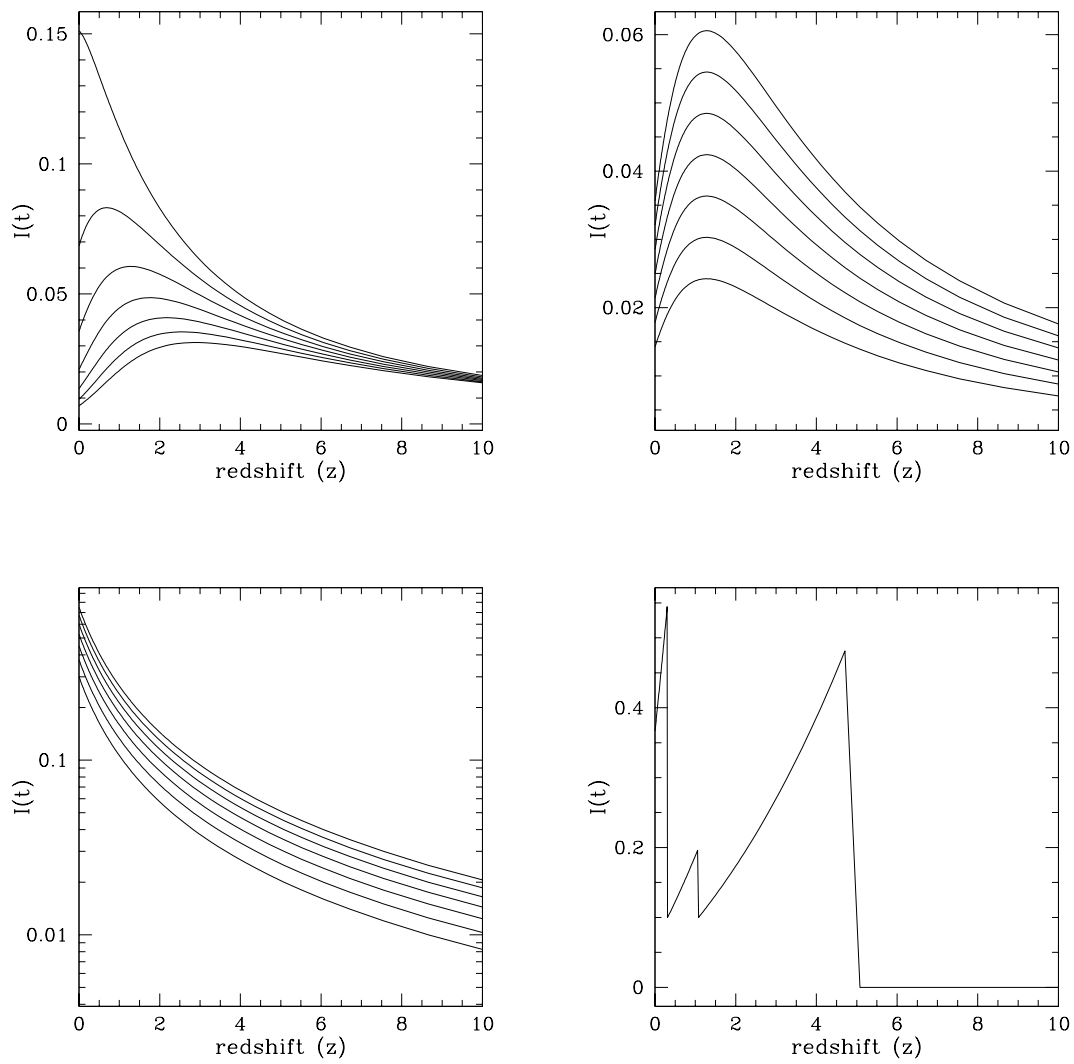


FIG. B19.— How the I parameter is predicted to change as a function of redshift in different galaxy evolution scenarios (see text).

REFERENCES

- Abraham, R.G., Valdes, F., Yee, H.K.C., & van den Bergh, S. 1994, *ApJ*, 432, 75
- Abraham, R.G., Tanvir, N.R., Santiago, B.X., Ellis, R.S., Glazebrook, K., & van den Bergh, S. 1996, *MNRAS*, 279, 47L
- Abraham, R.G., & van den Bergh, S. 2001, *Science*, 293, 1273
- Bershady, M.A., Jangren, J.A., & Conselice, C.J. 2000, *AJ*, 119, 2645
- Bertola, F., & Capaccioli, M. 1975, *ApJ*, 200, 439
- Blain, A.W., Jameson, A., Smail, I., Longair, M.S., Kneib, J.-P., & Ivison, R.J. 1999, *MNRAS*, 309, 715
- Block, D.L., & Puerari, I. 1999, *A&A*, 342, 627
- Borne, K.D., et al. 1999, *Ap&SS*, 266, 137
- Borne, K.D., Bushouse, H., Lucas, R.A., & Colina, L. 2000, *ApJ*, 529, L77
- Buta, R., & Combes, F. 1996, *Fund. Cosmic Phys.*, 17, 95
- Canalizo, G., & Stockton, A. 2001, *ApJ*, 555, 719
- Cole, S., Lacey, C.G., Baugh, C.M., & Frenk, C.S. 2000, *MNRAS*, 319, 168
- Conselice, C.J. 1997, *PASP*, 109, 1251
- Conselice, C.J., & Gallagher, J.S. 1999, *AJ*, 117, 75
- Conselice, C.J., Bershady, M.A., & Jangren, A. 2000a, *ApJ*, 529, 886
- Conselice, C.J., Bershady, M.A., & Gallagher, J.S. 2000b, *A&A*, 354, 21L
- Conselice, C.J., Gallagher, J.S., Calzetti, D., Homeier, N., & Kinney, A. 2000c, *AJ*, 119, 79
- Conselice, C.J., Gallagher, J.S., & Wyse, R.F.G. 2001, *ApJ*, 559, 791
- Conselice, C.J., Gallagher, J.S., & Wyse, R.F.G. 2002, *AJ*, 123, 2246
- Conselice, C.J., Gallagher, J.S., & Wyse, R.F.G. 2003, *AJ*, 125, 66
- Conselice, C.J., Bershady, M.A., Dickinson, M., & Papovich, C. 2003, in prep
- Courteau, S., de Jong, R.S., & Broeils, A.H. 1996, *ApJ*, 457, 73L
- Curtis, H.D. 1918, *Lick Obs. Pub.*, 13, 12
- de Jong, R.S. 1996, *A&A*, 313, 45
- de Vaucouleurs, G. 1959, *Handb. der Physik*, 53, 275
- de Vaucouleurs, G. 1961, *ApJS*, 5, 233
- Devereux, N., & Hameed, S. 1997, *AJ*, 113, 599
- Dickinson, M. et al. 1998, *BAAS*, 193, 7511
- Doi, M., Fukugita, M., & Okamura, S. 1993, *MNRAS*, 264, 832
- Ellis, R.S. 1997, *ARA&A*, 35, 389
- Eskridge, P.B., et al. 2000, *AJ*, 119, 536
- Ferguson, H.C., & Binggeli, B. 1994, *A&ARv*, 6, 67
- Franx, M., Illingworth, G., & de Zeeuw, T. 1991, *ApJ*, 383, 112
- Gallagher III, J.S., Hunter, D.A., & Tutukov, A.V. 1984, *ApJ*, 284, 544
- Giavalisco, M., Livio, M., Bohlin, R.C., Macchetto, F.D., Stecher, T.P. 1996, *AJ*, 112, 369
- Gilmore, G., Wyse, R.F.G., & Norris, J.E. 2002, *ApJ*, 574, 39L
- Glazebrook, K., Ellis, R., Santiago, B., & Griffiths, R. 1995, *MNRAS*, 275, 19L
- Graham, A.W., Trujillo, I., & Caon, N. 2001, *AJ*, 122, 1707
- Hameed, S., & Devereux, N. 1999, *AJ*, 118, 730
- Harris, J., Calzetti, D., Gallagher, J.S., Conselice, C.J., & Smith, D. 2001, *AJ*, 122, 3046
- Holmberg, E. 1958, *Lund Medd. II*, 136
- Hubble, E. 1926, *ApJ*, 64, 321
- Hubble, E. 1936, *The Realm of the Nebulae*, Yale University Press, New Haven
- Isserstedt, J., & Schindler, R. 1986, *A&A*, 167, 11
- Kent, S.M. 1985, *ApJS*, 59, 115
- Kennicutt, R.C. 1981, *AJ*, 86, 1847
- Kennicutt, R.C., & Kent, S.M. 1983, *AJ*, 88, 1094
- Kormendy, J., & Bender, R. 1996, *ApJ*, 464, 119L
- Lacey, C., & Cole, S. 1993, *MNRAS*, 262, 627L
- Lambas, D.G., Maddox, S.J., & Loveday, J. 1992, *MNRAS*, 258, 404
- Massey, R.J., Refregier, A.R., Conselice, C.J., & Bacon, D.J. 2003, *astro-ph/0301449*
- Morgan, W.W., & Mayall, N.U. 1957, *PASP*, 69, 291
- Morgan, W.W. 1958, *PASP*, 70, 364
- Morgan, W.W. 1959, *PASP*, 71, 394
- Morgan, W.W., & Osterbrock, D.E. 1969, *AJ*, 74, 515
- Naim, A., Lahav, O., Sodre, L., Storrie-Lombardi, M.C. 1995b, *MNRAS*, 275, 567
- Naim, A., et al. 1995a, *MNRAS*, 274, 1107
- Naim, A., Ratnatunga, K.U., & Griffiths, R.E. 1997, *ApJ*, 476, 510
- Odewahn, S.C., Cohen, S.H., Windhorst, R.A., & Philip, N.S. 2002, *ApJ*, 568, 539
- Okamura, S., Kodaira, K., & Watanabe, M. 1984, *ApJ*, 280, 7
- Peebles, P.J.E. 1980, "The large-scale structure of the universe", Princeton University Press, Princeton, N.J.
- Peng, C.Y., Ho, L.C., Impey, C.D., & Rix, H.-W. 2002, *AJ*, 124, 266
- Quinn, P.J., Hernquist, L., & Fullagar, D.P. 1993, *ApJ*, 403, 74
- Richter, O.-G., & Sancisi, R. 1994, *A&A*, 290, 9L
- Rieke, G.H., & Low, F.J. 1972, *ApJ*, 176, 95L
- Roberts, M.S., & Haynes, M.P. 1994, *ARA&A*, 32, 115
- Romanishin, W. 1990, *AJ*, 100, 373
- Ryden, B.S. 1996, *ApJ*, 461, 146
- Sancisi, R. 1976, *A&A*, 53, 159
- Sandage, A. 1975, in *Galaxies and the Universe*, eds. A. Sandage, M. Sandage & J. Kristien, U. Chicago Press, Chicago, 1
- Sandage, A. 1961, *The Hubble Atlas of Galaxies*, Carnegie Institute of Washington, Washington, D.C.
- Sandage, A., & Tammann, G.A. 1981, *Revised Shapley-Ames Catalog of Galaxies*, Carnegie Institution of Washington, Washington, D.C.
- Sandage, A. 1986, *A&A*, 161, 89
- Sanders, D.B., & Mirabel, I.F. 1996, *ARA&A*, 34, 749
- Sanders, D.B., Soifer, B.T., Elias, J.H., Madore, B.F., Matthews, K., Neugebauer, G., & Scoville, N.Z. 1988, 325, 74
- Schweizer, F., & Seitzer, P. 1992, *AJ*, 104, 1039
- Shade, D., Lilly, S.J., Crampton, D., Hammer, F., LeFevre, O., & Tresse, L. 1995, *ApJ*, 451, 1L
- Simard, L. et al. 2002, *ApJS*, 142, 1
- Sofue, Y., & Rubin, V. 2001, *ARA&A*, 39, 137
- Steinmetz, M., & Navarro, J.F. 2002, preprint, *astro-ph/0202466*
- van den Bergh, S. 1960, *ApJ*, 131, 215
- van den Bergh, S. 1998, *Galaxy Morphology and Classification*, Cambridge University Press, Cambridge
- van den Bergh, S., Cohen, J.G., & Crabbe, C. 2001, *AJ*, 122, 611
- van Zee, L. 2000, *AJ*, 119, 2757
- White, S.D.M., & Frenk, C.S. 1991, *ApJ*, 379, 52
- White, R.E. III, Keel, W.C., & Conselice, C.J. 2000, *ApJ*, 542, 761
- Williams, R.E. 1996, *AJ*, 112, 1335
- Windhorst, R.A. et al. 2002, *ApJS*, 143, 113
- Wright, G.S., James, P.A., Joseph, R.D., & McLean, I.S. 1990, *Nature*, 334, 417
- Zaritsky, D., & Rix, H.-W. 1997, *ApJ*, 477, 118
- Zwicky, F. 1957, "Morphological Astronomy", Berlin, Springer

TABLE 1
NEARBY NORMAL GALAXIES FROM THE FREI SAMPLE

NGC	Hubble Type	M_B	$C(R)^A$	$A(R)$	$A_G(R)$	$S(R)$
2403	SABcd	-20.5	2.87	0.12±0.04	0.09±0.00	0.40±0.04
2541	SAcd	-19.0	3.16	0.01±0.13	0.15±0.01	0.23±0.01
2683	SAb	-19.8	3.31	0.17±0.01	0.13±0.00	0.43±0.00
2715	SABc	-20.6	3.01	0.17±0.02	0.14±0.00	0.44±0.01
2768	S0	-22.1	4.39	0.02±0.01	0.03±0.00	0.08±0.01
2775	Scd	-21.1	4.30	0.07±0.01	0.08±0.00	0.07±0.01
2903	SABbc	-20.3	3.06	0.12±0.01	0.03±0.00	0.38±0.00
2976	SAc	-16.7	2.50	0.09±0.02	0.06±0.00	0.31±0.01
2985	SAab	-21.5	4.49	0.06±0.02	0.05±0.00	0.01±0.01
3031	SAab	-19.2	3.95	0.07±0.01	0.03±0.00	0.09±0.00
3077	I0	-17.0	3.54	0.19±0.01	0.18±0.00	0.09±0.00
3079	SBc	-21.9	4.06	0.43±0.01	0.30±0.00	0.86±0.01
3147	SAbc	-22.6	4.00	0.07±0.02	0.07±0.00	0.06±0.01
3166	SA0/a	-21.4	4.44	0.07±0.00	0.06±0.00	0.16±0.01
3184	SABcd	-20.2	2.36	0.14±0.04	0.12±0.01	0.23±0.00
3198	SBc	-20.2	3.01	0.05±0.05	0.02±0.01	0.31±0.00
3319	SBcd?	-19.7	2.99	0.05±0.13	0.18±0.00	0.00±0.01
3344	SABbc	-19.3	3.08	0.21±0.01	0.18±0.00	0.39±0.01
3351	SBb	-20.1	4.05	0.06±0.01	0.03±0.00	0.10±0.00
3368	SABab	-20.4	4.01	0.06±0.01	0.06±0.00	0.01±0.00
3377	E5-6	-19.4	4.84	0.04±0.01	0.03±0.00	-0.03±0.01
3379	E1	-20.2	4.61	0.02±0.01	0.02±0.00	0.01±0.01
3486	SABc	-19.3	3.59	0.13±0.02	0.08±0.00	0.25±0.01
3556	SBcd	-20.9	2.97	0.24±0.01	0.15±0.00	0.51±0.01
3596	SABc	-21.0	2.93	0.14±0.01	0.12±0.00	0.21±0.01
3623	SABa	-20.7	3.92	0.11±0.01	0.07±0.00	0.22±0.01
3631	SAc	-21.6	3.70	0.13±0.02	0.16±0.00	0.24±0.01
3672	SAc	-21.2	3.10	0.22±0.01	0.17±0.00	0.39±0.01
3675	SAb	-20.2	3.68	0.12±0.02	0.12±0.00	0.07±0.01
3726	SABc	-21.1	2.49	0.23±0.04	0.21±0.00	0.22±0.01
3810	SAc	-20.8	3.43	0.18±0.01	0.13±0.00	0.32±0.01
3877	SAc	-20.3	3.44	0.19±0.01	0.15±0.00	0.47±0.01
3893	SABc	-21.0	3.22	0.19±0.01	0.15±0.00	0.25±0.01
3938	SAc	-21.1	2.97	0.17±0.02	0.15±0.00	0.33±0.04
3953	SBbc	-21.2	3.67	0.11±0.02	0.10±0.00	0.21±0.01
4013	Sb	-19.8	3.65	-0.03±0.10	0.06±0.01	0.59±0.03
4030	SAbc	-21.6	3.67	0.11±0.01	0.05±0.00	0.18±0.01
4088	SABbc	-20.9	2.63	0.37±0.01	0.28±0.00	0.64±0.01
4123	SBbc	-21.0	2.92	0.11±0.03	0.12±0.00	0.22±0.01
4125	E6	-22.1	4.60	-0.02±0.03	0.11±0.01	-0.02±0.01
4136	SABc	-19.2	2.97	0.09±0.03	0.10±0.00	0.25±0.01
4144	SABcd?	-16.9	3.98	0.13±0.04	0.18±0.00	0.30±0.01
4157	SABb?	-20.9	3.93	0.28±0.02	0.30±0.00	0.21±0.01
4178	SAdm	-20.1	2.87	0.10±0.06	0.14±0.00	0.55±0.01
4189	SABcd?	-19.6	2.46	0.26±0.03	0.18±0.00	0.37±0.01
4192	SABab	-21.3	3.63	0.19±0.03	0.11±0.00	0.36±0.00
4216	SABb	-21.2	5.08	0.17±0.01	0.07±0.00	0.38±0.00
4242	SABdm	-18.8	2.50	0.09±0.04	0.11±0.02	0.21±0.01
4254	SAc	-21.8	3.32	0.29±0.02	0.20±0.00	0.49±0.00
4258	SAc	-20.9	3.50	0.15±0.02	0.12±0.00	0.19±0.00
4303	SABbc	-21.6	2.79	0.24±0.02	0.14±0.00	0.51±0.00
4321	SABbc	-21.9	2.91	0.12±0.02	0.07±0.01	0.28±0.00
4340	SB0	-20.0	4.55	0.00±0.01	0.03±0.00	-0.02±0.01
4365	E3	-21.5	4.53	0.02±0.01	0.02±0.00	-0.01±0.01
4374	E1	-22.0	4.48	0.01±0.01	0.01±0.00	-0.03±0.01
4394	SBb	-20.4	4.40	0.02±0.02	0.08±0.00	0.00±0.00
4406	S0/E3	-22.0	4.17	0.01±0.01	0.03±0.00	-0.03±0.01

^ATypically errors on the concentration index are $\pm C = 0.1$.

TABLE 1
NEARBY NORMAL GALAXIES FROM THE FREI SAMPLE

NGC	Hubble Type	M_B	$C(R)^A$	$A(R)$	$A_G(R)$	$S(R)$
4414	SAc?	-19.8	3.50	0.13±0.01	0.05±0.00	0.35±0.01
4429	SA0	-21.0	4.05	0.06±0.01	0.07±0.00	0.08±0.01
4442	SB0	-20.7	3.99	0.05±0.00	0.04±0.00	0.03±0.01
4449	IBm	-18.2	3.08	0.24±0.01	0.20±0.00	0.40±0.01
4450	SAab	-21.1	3.93	0.02±0.02	0.06±0.00	-0.04±0.01
4472	E2/S0	-22.7	4.17	0.01±0.01	0.03±0.00	0.01±0.00
4477	SB0	-20.7	4.50	0.02±0.01	0.04±0.00	-0.01±0.01
4486	E2	-22.5	4.00	0.00±0.01	0.01±0.00	0.02±0.00
4487	SABcd	-20.8	2.85	0.09±0.04	0.14±0.00	0.18±0.01
4498	SABd	-19.3	3.03	0.08±0.05	0.12±0.00	0.35±0.01
4501	SAb	-21.8	3.22	0.13±0.01	0.08±0.00	0.20±0.00
4526	SAB0	-21.5	3.96	0.05±0.01	0.04±0.00	0.02±0.01
4527	SABbc	-20.2	3.92	0.16±0.02	0.04±0.00	0.32±0.00
4535	SABc	-21.5	2.54	0.12±0.04	0.10±0.00	0.40±0.00
4548	SBb	-21.1	3.71	0.00±0.03	0.07±0.00	0.03±0.00
4559	SABcd	-20.5	3.13	0.10±0.04	0.14±0.00	0.35±0.00
4564	E6	-20.1	4.58	0.04±0.01	0.04±0.00	-0.02±0.01
4569	SABcd	-21.8	3.36	0.08±0.03	0.09±0.00	0.16±0.00
4571	SAd	-20.2	2.69	0.00±0.06	0.08±0.00	0.07±0.01
4579	SABb	-21.6	4.04	0.03±0.02	0.05±0.00	0.06±0.00
4593	SBb	-22.3	4.32	0.08±0.02	0.12±0.00	0.14±0.01
4594	E6	-23.9	3.98	0.13±0.02	0.09±0.00	0.53±0.01
4621	SAc	-21.5	4.64	0.00±0.01	0.01±0.00	-0.06±0.01
4636	E/S0	-21.6	4.18	0.02±0.01	0.01±0.00	-0.06±0.01
4651	SAc	-20.7	3.53	0.08±0.02	0.06±0.00	0.16±0.00
4654	SABcd	-20.9	2.83	0.11±0.05	0.17±0.00	0.17±0.04
4689	SAbc	-20.5	3.05	0.03±0.08	0.05±0.01	0.08±0.01
4710	SA0	-20.2	3.50	0.05±0.01	0.04±0.00	0.63±0.01
4725	SABab	-21.4	3.72	0.02±0.04	0.05±0.01	0.09±0.01
4731	SBcd	-21.2	3.06	0.21±0.05	0.20±0.00	0.57±0.01
4754	SB0	-20.7	4.75	0.01±0.01	0.02±0.00	-0.03±0.01
4826	SAab	-20.0	3.19	0.11±0.02	0.09±0.00	0.03±0.01
4861	SBm	-19.5	3.05	0.11±0.09	0.17±0.01	0.07±0.02
4866	SA0	-20.2	4.57	0.01±0.03	0.08±0.00	0.24±0.01
5005	SABbc	-21.9	4.16	0.11±0.01	0.09±0.00	0.22±0.01
5033	SAc	-21.5	4.53	0.11±0.04	0.09±0.00	0.24±0.01
5055	SAbc	-20.8	3.54	0.09±0.02	0.05±0.00	0.21±0.00
5204	SAm	-17.6	3.03	0.32±0.04	0.47±0.00	0.26±0.01
5248	SABbc	-21.8	3.46	0.16±0.01	0.14±0.00	0.26±0.01
5322	E3-4	-22.3	4.67	0.02±0.01	0.02±0.00	-0.01±0.01
5334	SBc	-21.0	2.58	0.04±0.11	0.13±0.01	0.14±0.02
5364	SAbc	-21.8	3.15	0.12±0.03	0.16±0.00	0.27±0.01
5371	SAbc	-22.5	3.06	0.13±0.02	0.13±0.00	0.21±0.01
5377	SBa	-21.1	4.55	0.03±0.01	0.07±0.00	0.00±0.01
5585	SABd	-18.8	3.03	0.23±0.02	0.27±0.00	0.24±0.01
5669	SABcd	-20.9	3.05	0.18±0.03	0.22±0.00	0.31±0.01
5701	SB0/a	-21.3	4.11	0.04±0.01	0.05±0.00	0.06±0.01
5746	SABb	-22.6	4.33	0.27±0.01	0.15±0.00	0.57±0.01
5792	SBb	-21.4	3.63	0.28±0.02	0.26±0.00	0.29±0.01
5813	E1-2	-21.7	4.30	0.01±0.02	0.03±0.00	-0.01±0.01
5850	SBb	-21.7	4.35	0.05±0.02	0.10±0.00	0.02±0.01
5985	SABb	-22.1	2.88	0.14±0.02	0.16±0.00	0.20±0.01
6015	SAc	-20.5	2.95	0.12±0.02	0.10±0.00	0.37±0.01
6118	SAc	-21.1	2.72	0.09±0.03	0.12±0.00	0.24±0.01
6384	SAbc	-22.1	3.72	0.14±0.01	0.09±0.00	0.24±0.01
6503	SAc	-19.5	3.06	0.16±0.01	0.12±0.00	0.38±0.00

^ATypically errors on the concentration index are $\pm C = 0.1$.

TABLE 2
STARBURST GALAXIES

Name	M_B	$C(R)^A$	$A(R)$	$A_G(R)$	$S(R)$
Mrk8	-20.3	2.45	0.55 ± 0.01	0.36 ± 0.00	0.94 ± 0.00
NGC3310	-20.3	2.97	0.31 ± 0.00	0.12 ± 0.00	0.48 ± 0.01
NGC3690	-21.1	2.63	0.86 ± 0.01	0.32 ± 0.00	0.80 ± 0.00
NGC7673	-21.4	2.98	0.58 ± 0.00	0.42 ± 0.00	0.53 ± 0.10
NGC7678	-21.6	2.55	0.34 ± 0.01	0.23 ± 0.00	0.48 ± 0.00

^ATypically errors on the concentration index are $\pm C = 0.1$.

TABLE 3
 DWARF ELLIPTICALS FROM CONSELICE ET AL. (2003)

ID ^A	M _B	C(R) ^B	A(R)	A _G (R)	S(R)
1	-13.8	2.29	-0.01±0.08	0.01±0.02	-0.01±0.06
2	-14.3	2.30	0.09±0.04	0.13±0.01	0.03±0.04
4	-13.6	2.67	0.01±0.03	0.04±0.01	-0.06±0.04
6	-14.3	2.47	0.03±0.03	0.05±0.01	0.03±0.04
8	-14.7	2.14	0.01±0.03	0.01±0.01	0.03±0.03
9	-13.0	2.15	0.01±0.12	0.03±0.04	-0.02±0.07
15	-14.0	2.32	0.00±0.06	0.00±0.02	-0.02±0.05
16	-14.6	2.52	0.04±0.02	0.05±0.01	-0.01±0.03
17	-13.5	2.46	-0.01±0.04	-0.01±0.01	-0.04±0.04
19	-13.8	2.91	0.04±0.03	0.05±0.01	0.00±0.04
29	-13.4	2.30	0.02±0.05	0.02±0.01	0.05±0.04
30	-13.0	2.78	0.02±0.04	0.05±0.02	0.00±0.05
32	-14.2	2.97	-0.01±0.04	0.04±0.01	-0.19±0.05
37	-13.6	1.90	0.05±0.01	0.06±0.00	0.00±0.02
38	-15.9	2.48	0.02±0.01	0.02±0.00	0.01±0.02
39	-15.7	2.68	0.01±0.01	0.01±0.00	0.03±0.02
40	-15.1	2.57	0.02±0.01	0.03±0.00	-0.01±0.02
45	-15.7	2.40	0.02±0.01	0.03±0.00	0.01±0.02
47	-13.5	2.65	0.01±0.03	0.01±0.01	0.03±0.04

^AThese identification numbers are from Conselice, Gallagher & Wyse (2003).

^BTypically errors on the concentration index are $\pm C = 0.1$.

TABLE 4
DWARF IRREGULARS FROM VAN ZEE (2000)

Name	$C(B)^A$	$A(B)$	$A_G(B)$	$S(B)$
UGC00191	2.78	0.27±0.04	0.30±0.00	0.43±0.02
UGC00290	3.30	0.08±0.07	-0.05±0.03	0.55±0.06
UGC00634	2.78	0.15±0.08	0.06±0.01	0.59±0.03
UGC00685	2.77	0.17±0.03	0.12±0.00	0.35±0.02
UGC00891	2.74	0.08±0.06	0.07±0.00	0.29±0.02
UGC01104	2.94	0.21±0.01	0.13±0.00	0.33±0.02
UGC01175	2.66	0.25±0.04	0.23±0.01	0.22±0.05
UGC01281	3.08	0.09±0.05	0.17±0.00	0.81±0.01
UGC01501	3.18	0.26±0.02	0.15±0.00	0.95±0.01
UGC02345	2.53	0.16±0.09	0.18±0.02	0.44±0.02
UGC02603	2.57	0.20±0.12	0.21±0.01	0.52±0.05
UGC03647	2.97	0.11±0.08	0.16±0.01	0.53±0.02
UGC04117	2.87	0.27±0.03	0.18±0.00	0.45±0.03
UGC05205	2.66	0.23±0.03	0.16±0.00	0.23±0.03
UGC05288	3.03	0.24±0.02	0.11±0.00	0.65±0.02
UGC09128	2.51	0.24±0.04	0.21±0.00	0.36±0.02
UGC09211	3.09	0.17±0.13	0.40±0.01	0.26±0.02
UGC09219	2.78	0.35±0.02	0.22±0.00	0.54±0.02
UGC09240	2.49	0.25±0.02	0.17±0.00	0.51±0.01
UGC09500	2.97	0.03±0.11	0.07±0.02	0.27±0.03
UGC09992	3.15	0.10±0.06	0.10±0.01	0.40±0.03
UGC10054	2.92	0.11±0.04	0.10±0.01	0.47±0.02
UGC10310	2.44	0.24±0.05	0.17±0.00	0.54±0.02
UGC10351	3.05	0.17±0.01	0.11±0.00	0.34±0.03
UGC10445	2.52	0.30±0.02	0.13±0.00	0.60±0.01
UGC10669	2.81	-0.09±0.18	0.27±0.01	-0.07±0.05
UGC10805	2.80	0.28±0.05	0.28±0.00	0.40±0.03
UGC10991	2.78	0.45±0.05	0.46±0.01	0.86±0.04
UGC11755	3.91	0.16±0.01	0.09±0.00	0.37±0.02
UGC11782	3.05	0.09±0.07	0.08±0.01	0.36±0.02
UGC11944	3.41	0.14±0.07	0.18±0.00	0.26±0.03
UGC12613	2.98	0.04±0.12	0.20±0.01	0.26±0.01
UGC12713	2.90	0.18±0.01	0.10±0.00	0.29±0.02
UGCA009	2.76	0.02±0.07	0.09±0.01	0.25±0.02
UGCA015	2.43	0.11±0.09	0.12±0.01	0.33±0.04
UGCA433	3.16	0.09±0.11	0.22±0.01	0.23±0.03
UGCA439	2.98	0.14±0.00	0.09±0.00	0.27±0.03

^ATypically errors on the concentration index are $\pm C = 0.1$.

TABLE 5
IRAS INFRARED GALAXIES

Number ^A	Name	Redshfit	$C(I,V)^{B,C}$	$A(I,V)^C$	$A_G(I,V)^C$	$S(I,V)^C$
1	IRAS00060 - 1543	0.195	3.85	0.34±0.04	0.38±0.00	0.51± 0.06
2	IRAS00091 - 0738	0.118	3.13	0.32±0.03	0.24±0.00	0.42± 0.04
3	IRAS00104 - 0139	0.163	4.16	0.52±0.03	0.24±0.01	0.35± 0.06
4	IRAS00161 - 0850	0.109	3.13	0.32±0.03	0.20±0.00	0.42± 0.04
5	IRAS00335 - 2732	0.069	3.66	0.18±0.00	0.11±0.00	0.33± 0.03
6	IRAS00456 - 2904	0.110	3.05	0.23±0.01	0.11±0.00	0.46± 0.03
7	IRAS00509 + 1225	0.061	3.44	0.22±0.00	0.10±0.00	1.09± 0.02
8	IRAS00589 - 0352	0.176	3.83	0.36±0.01	0.23±0.00	0.29± 0.04
9	IRAS01031 - 2255	0.187	3.52	0.30±0.01	0.22±0.00	0.20± 0.07
10	IRAS01199 - 2307	0.156	4.31	0.29±0.02	0.21±0.00	0.23± 0.06
11	IRAS01355 - 1814	0.192	2.46	0.42±0.04	0.46±0.00	0.43± 0.07
12	IRAS01579 - 1925	0.173	3.89	0.08±0.01	0.06±0.00	0.13± 0.03
13	IRAS02021 - 2104	0.116	3.92	0.20±0.03	0.16±0.00	0.22± 0.03
14	IRAS02130 - 1948	0.192	3.02	0.59±0.02	0.35±0.00	0.69± 0.04
15	IRAS02364 - 4751	0.098	3.66	0.27±0.02	0.15±0.00	0.56± 0.03
16	IRAS02459 - 0233	0.180	3.62	0.71±0.02	0.22±0.00	0.74± 0.03
17	IRAS06035 - 7102	0.079	2.54	0.63±0.06	0.36±0.01	0.86± 0.02
18	IRAS06206 - 6315	0.092	2.76	0.11±0.07	0.24±0.01	0.50± 0.03
19	IRAS09320 + 6134	0.039	3.78	0.16±0.02	0.10±0.00	0.24± 0.01
20	IRAS09425 + 1751	0.128	5.53	0.23±0.01	0.19±0.00	0.09± 0.03
21	IRAS09427 + 1929	0.149	2.54	0.20±0.02	0.18±0.00	0.32± 0.07
22	IRAS11095 - 0238	0.107	3.03	0.35±0.02	0.28±0.00	0.48± 0.05
23	IRAS12112 + 0305	0.073	3.45	0.54±0.04	0.54±0.00	0.85± 0.02
24	IRAS12450 + 3401	0.159	3.54	0.52±0.04	0.58±0.00	0.87± 0.05
25	IRAS13349 + 2438	0.108	3.45	0.28±0.00	0.15±0.00	1.36± 0.02
26	IRAS13428 + 5608	0.038	3.23	0.29±0.01	0.18±0.00	0.47± 0.01
27	IRAS14348 - 1447	0.082	3.52	0.36±0.03	0.37±0.00	0.99± 0.02
28	IRAS14378 - 3651	0.068	4.01	0.20±0.01	0.15±0.00	0.13± 0.03
29	IRAS15250 + 3609	0.055	2.94	0.44±0.02	0.32±0.00	0.58± 0.02
30	IRAS15327 + 2340	0.018	2.99	0.27±0.02	0.21±0.01	0.35± 0.01
31	IRAS16007 + 3743	0.185	2.56	0.89±0.03	0.91±0.00	1.34± 0.04
32	IRAS17208 - 0014	0.043	2.77	0.36±0.01	0.19±0.00	0.75± 0.02
33	IRAS19254 - 7245	0.062	3.67	0.62±0.02	0.29±0.00	0.46± 0.01
34	IRAS19297 - 0406	0.086	5.59	0.41±0.02	0.66±0.01	1.38± 0.03
35	IRAS22088 - 1831	0.170	3.13	0.32±0.03	0.25±0.00	0.42± 0.04
36	IRAS22206 - 2715	0.131	3.84	0.67±0.04	0.66±0.00	0.55± 0.03
37	IRAS22509 - 0040	0.058	3.62	0.42±0.01	0.15±0.00	0.54± 0.02
38	IRAS22546 - 2637	0.164	3.82	0.58±0.04	0.54±0.00	0.57± 0.05
39	IRAS23146 - 1116	0.101	3.71	0.36±0.01	0.28±0.00	0.92± 0.04
40	IRAS23242 - 0357	0.189	4.73	0.19±0.01	0.12±0.00	0.15± 0.06
41	IRAS23410 + 0228	0.091	5.62	0.51±0.01	0.47±0.00	0.15± 0.03
42	IRAS23515 - 2421	0.153	2.87	0.39±0.01	0.27±0.00	0.44± 0.04
43	IRAS23574 - 2355	0.144	3.12	0.38±0.07	0.47±0.01	0.28± 0.05
44	IRAS00275 - 2859	0.280	3.73	0.35±0.00	0.35±0.00	0.00± 0.04
45	IRAS02054 + 0835	0.345	3.64	0.43±0.00	0.43±0.00	0.00± 0.05
46	IRAS02587 - 6336	0.255	4.05	0.25±0.02	0.19±0.01	0.12± 0.09
47	IRAS04384 - 4848	0.204	2.83	0.29±0.10	0.34±0.01	0.41± 0.06
48	IRAS06268 + 3509	0.170	3.16	0.40±0.10	0.48±0.01	0.45± 0.05
49	IRAS06361 - 6217	0.160	3.32	0.17±0.08	0.43±0.06	0.43± 0.06
50	IRAS06561 + 1902	0.188	4.37	0.06±0.06	0.46±0.01	0.51± 0.04
51	IRAS07381 + 3215 ^D	0.170	2.80	0.17±0.09	0.29±0.01	0.17± 0.09
52	IRAS10026 + 4347	0.178	3.38	0.24±0.00	0.24±0.00	0.00± 0.03
53	IRAS10579 + 0438	0.173	3.04	0.13±0.09	0.17±0.01	0.02± 0.08
54	IRAS13469 + 5833	0.158	3.24	0.11±0.13	0.30±0.01	0.11± 0.04
55	IRAS14337 - 4134	0.182	2.98	0.33±0.02	0.96±0.01	2.00± 0.04
56	IRAS16159 - 0402	0.213	3.75	0.13±0.14	0.62±0.01	0.18± 0.07
57	IRAS17431 - 5157	0.175	3.17	-0.05±0.20	0.19±0.04	0.00± 0.01
58	IRAS18520 - 5048	0.152	3.39	0.38±0.05	0.42±0.00	0.44± 0.04
59	IRAS18580 + 6527	0.176	4.07	0.57±0.02	0.85±0.00	1.74± 0.03
60	IRAS20037 - 1547	0.192	3.31	0.28±0.07	0.43±0.02	0.42± 0.05
61	IRAS20109 - 3003	0.143	2.89	0.24±0.06	0.25±0.01	0.20± 0.05
62	IRAS20176 - 4756	0.178	2.61	0.01±0.11	0.15±0.01	0.30± 0.07
63	IRAS20253 - 3757	0.180	4.11	0.43±0.04	0.49±0.00	0.70± 0.05
64	IRAS20507 - 5412	0.228	3.04	0.21±0.05	0.19±0.01	0.34± 0.10
65	IRAS23140 + 0348	0.220	6.04	0.13±0.01	0.13±0.00	0.06± 0.04
66	IRAS23220 + 2919	0.240	4.32	0.22±0.03	0.19±0.01	0.13± 0.11

^AID number corresponds to the galaxy images shown in Figure 2.

^BTypically errors on the concentration index are $\pm C = 0.1$.

^CFor objects 1-43, the parameters listed are measured in the F814W filter and for objects 44-66 the F606W filter was used (see §3.4).

^DIRAS07381 + 3215 due to its lower than average surface brightness had its parameters measured within the $3 \times r(\eta = 0.5)$ radius.

TABLE 6
 AVERAGES AND 1σ VARIATIONS OF STRUCTURAL PARAMETERS FOR GALAXY TYPES

Type	$C(R)$	$A(R)$	$S(R)$
Ellipticals	4.4 ± 0.3	0.02 ± 0.02	0.00 ± 0.04
Early-Type Disks (Sa - Sb)	3.9 ± 0.5	0.07 ± 0.04	0.08 ± 0.08
Late-Type Disks (Sc - Sd)	3.1 ± 0.4	0.15 ± 0.06	0.29 ± 0.13
Irregulars	2.9 ± 0.3	0.17 ± 0.10	0.40 ± 0.20
Edge-On Disks	3.7 ± 0.6	0.17 ± 0.11	0.45 ± 0.20
ULIRGs	3.5 ± 0.7	0.32 ± 0.19	0.50 ± 0.40
Starbursts	2.7 ± 0.2	0.53 ± 0.22	0.74 ± 0.25
Dwarf Ellipticals	2.5 ± 0.3	0.02 ± 0.03	0.00 ± 0.06

TABLE 7
 AVERAGE CHANGE IN CAS PARAMTERS FROM REDSHIFT EFFECTS

z	$\delta C(z)$	GOODS ACS $\delta A(z)$	$\delta S(z)$	$\delta C(I)$	HDF WFPC2 $\delta A(I)$	$\delta S(I)$	z	$\delta C(B_{\text{rest}})$	HDF NICMOS $\delta A(B_{\text{rest}})$	$\delta S(B_{\text{rest}})$
0.5	0.08 ± 0.15	0.00 ± 0.06	-0.17 ± 0.41	0.09 ± 0.19	-0.01 ± 0.07	-0.20 ± 0.17	1.0	0.01 ± 0.04	-0.14 ± 0.08	-0.19 ± 0.12
1.0	0.10 ± 0.18	-0.03 ± 0.07	-0.25 ± 0.43	0.10 ± 0.23	-0.01 ± 0.08	-0.25 ± 0.19	1.5	-0.01 ± 0.02	-0.11 ± 0.06	-0.15 ± 0.13
2.0	0.06 ± 0.24	-0.10 ± 0.10	-0.32 ± 0.47	0.11 ± 0.23	-0.03 ± 0.10	-0.30 ± 0.22	2.0	0.01 ± 0.09	-0.23 ± 0.12	-0.25 ± 0.20
3.0	0.06 ± 0.40	-0.14 ± 0.13	-0.30 ± 0.56	0.09 ± 0.22	-0.09 ± 0.12	-0.34 ± 0.24	3.0	-0.08 ± 0.23	-0.36 ± 0.14	-0.37 ± 0.45